RTTOV-8 - SCIENCE AND VALIDATION REPORT

Roger Saunders
Met Office

with contributions from

Pascal Brunel, Stephen English, Peter Bauer, Una O'Keeffe, Peter Francis and Peter Rayer

This documentation was developed within the context of the EUMETSAT Satellite Application Facility on Numerical Weather Prediction (NWP SAF), under the Cooperation Agreement dated 25 November 1998, between EUMETSAT and The Met Office, UK, by one or more partners within the NWP SAF. The partners in the NWP SAF are The Met. Office, ECMWF, KNMI and Météo France.

Change record			
Version	Date	Author / changed by	Remarks
1.1	21 Feb 05	R W Saunders	Draft version for comments by authors
1.2	2 Mar 05	R W Saunders	Version amended after comments from authors
1.3	18 Aug 05	R W Saunders	Section on jacobian validation added and changes made to RTTOV_SCATT section
1.4	13 Oct 05	R W Saunders	Added AMSU-A jacobians + more on SCATT
1.5	16 Jan 06	U. O'Keeffe	Updated RTTOV_SCATT section
1.6	2 Feb 06	R W Saunders	Amended after comments from Marco

1. Introduction and Documentation

The purpose of this report is to document the scientific aspects of the latest version of the NWP SAF fast radiative transfer model, referred to hereafter as RTTOV-8, which are different from the previous model RTTOV-7 and present the results of the validation tests which have been carried out. The enhancements to this version, released in November 2004, have been made as part of the activities of the EUMETSAT NWP-SAF. The RTTOV-8 software is available to users on request from the NWP SAF (email: mailto:nwpsaf@metoffice.gov.uk). The RTTOV-8 documentation can be viewed on the NWP SAF web site at: http://www.metoffice.gov.uk/research/interproj/nwpsaf/rtm/ which may be updated from time to time. Technical documentation about the software can be found in the RTTOV-8 user's guide which is also available and can be downloaded from the RTTOV web site at the link above. The November 2004 versions of the documentation are included in the RTTOV-8 distribution file.

The baseline document for the original version of RTTOV is available from ECWMF as Eyre (1991). This was updated for RTTOV-5 (Saunders *et. al.* 1999a, Saunders *et. al.*, 1999b) and for RTTOV-6 with the RTTOV-6 science and validation report hereafter referred to as R6REP2000 and for RTTOV-7 with the RTTOV-7 science and validation report hereafter referred to as R7REP2002 both available from the NWP SAF web site at the link above. The changes described here only relate to the scientific differences from RTTOV-7. For details on the technical changes to the software, user interface etc. the reader is referred to the RTTOV-8 user manual. In summary the two major technical changes are a complete rewrite of the code using the features of FORTRAN-90 and an option in the coefficient file ingest to read binary files which significantly speeds up reading coefficient files for the advanced sounders with > 1000 channels.

2. Scientific Changes from RTTOV-7 to RTTOV-8

2.1 Changes to computation of gaseous transmittances

The original basis for the RTTOV fast computation of transmittances is based on Eyre and Woolf (1988). This was successively modified for RTTOV by Eyre (1991), Rayer (1995), Rizzi and Matricardi (1998), Saunders *et. al.* (1999) and Matricardi *et. al.* (2004) to the point that forward model computed transmittances are at an accuracy below the instrument noise of most sensors for RTTOV-7. However use of RTTOV-7 in NWP data assimilation runs have demonstrated that in some cases of extreme water vapour profiles anomalous values in the water vapour jacobians have been seen especially for AIRS simulations but also noted in AMSU-A simulations. This has provided motivation to update the water vapour transmittance computation. Another motivation is that the new line-by-line transmittances provide the option of separating the water vapour line and continuum absorption which allows for a more flexible update of the spectroscopic datasets. A third motivation is the requirement to simulate

IASI radiances which are at much higher spectral resolution than previous sensors simulated by RTTOV. As a result RTTOV-8 has been provided with 2 options for computing the atmospheric transmittance, that used in RTTOV-7 for backward compatibility and a new scheme in RTTOV-8 based on the predictors of Matricardi. (2003) used in RTIASIv4 and the updated set of line by line transmittances recently computed described below. These new predictors are still under development to trade off speed and accuracy and so for the initial release of RTTOV-8 only coefficient files for the old RTTOV-7 predictors were provided. The code is designed to read the coefficient file provided to decide which predictors should be used.

The simulation of transmittances in RTTOV is based on a regression scheme with a variety of predictors from the profile variables which are related to the layer optical depth, ($d_{i,j}$ - $d_{i,j-1}$), where $d_{i,j}$ is the level to space optical depth from level *j* and channel *i*. The regression is actually performed in terms of its departure from a reference profile, for mixed gases, water vapour, ozone etc. For RTTOV-7 and 8 the formulation is:

$$d_{i,j} = d_{i,j-1} + \sum_{k=1}^{K} a_{i,j,k} X_{k,j} \qquad (1)$$

where *K* is the number of predictors and their definitions (i.e. $X_{k,j}$) are given in Table 1 for the RTTOV-7 predictors and Tables 2 and 3 for the RTTOV-8 predictors with Table 4 giving the definition of the terms used in the predictors. $a_{i,j,k}$ are the regression coefficients provided in the coefficient files with each release of RTTOV. For RTTOV-8 predictors two new variable gases have been added (i.e. water vapour continuum and carbon dioxide). The new predictors given in Tables 2 and 3 are described in more detail in Matricardi (2003). For the mixed gases there are now 8 predictors, for water vapour line 12, water vapour continuum 4, ozone 11 and carbon dioxide 10. The latter 2 variable gases are optional and the computation can be turned off with a logical switch (e.g. ozone is currently off for all microwave channels). The trade off between model accuracy and the increasing cost of running the model is a future area of research to see if some of the predictors can be removed without significant loss in accuracy. The user selects which set of predictors to use (RTTOV-7 or 8) by providing the appropriate coefficient file.

One weakness of RTTOV simulations in general is that the near monochromatic assumption breaks down for wide spectral channels (e.g. SEVIRI 3.9μm channel) and this results in significant biases in the RTTOV simulations for these channels. This bias is removed at NWP centres by a bias correction scheme (e.g. Harris and Kelly, 2001). To help reduce this bias the conventional transmittances, $\tau_j(\nu)$ are weighted by the Planck function as defined by:

$$\tau_j^{PW} = \frac{\int \phi(\nu) B(\nu, T_j) \tau_j(\nu) d\nu}{\int \phi(\nu) B(\nu, T_j) d\nu} \qquad (2)$$

where τ_j^{PW} is the Planck weighted transmittance and $B(\nu, T)$ is the Planck function for a frequency ν and temperature *T* for a level *j*. Using these modified transmittances to compute the RT coefficients in the usual way results in a 'Planck weighted' coefficient

file that can be used by RTTOV in place of the conventional one. More details on the performance of the RTTOV-7/8 models using these 'Planck weighted' coefficient files can be found in Brunel and Turner (2003).

2.2 Improved microwave surface emissivity model, FASTEM-3

For RTTOV-7 Deblonde and English (2001) developed an improved version called FASTEM-2 which does a better job, than FASTEM-1, of taking into account the treatment of non-specular reflection within RTTOV. This has significantly improved the simulation of ocean surface emissivity for SSM/I and AMSU for larger viewing angles as described in Deblonde (2000).

For RTTOV-8 FASTEM-2 has been further updated to allow for the dependence of the ocean surface emissivity on the azimuth angle between the wind direction and the line of sight of the instrument. At the same time FASTEM has had coefficients added to predict the behaviour of the 3rd and 4th elements of the Stokes vector as a function of wind speed and wind direction. These changes allow the simulation of polarimetric microwave radiometer radiances (e.g. Windsat). This new version of the model has been called FASTEM-3. No other aspect of FASTEM-2 has been changed other than to switch off computations of the effects of roughness if the incidence angle exceeds 60 degrees and to correct the permittivity calculation in the original version of FASTEM-2. Incidence angles greater than 60 degrees are a rare event, but did occur briefly for the Aqua AMSU-A during platform manoeuvres and so the change made ensures the code does not crash for larger incidence angles.

To allow for the azimuthal variation of emissivity the method used was based on the empirical model of Fuzhong Weng (NOAA/NESDIS) in his routine "OceanEM" which was based on measurements by the WindRad radiometer operated by JPL, and is itself based on a model by St. Germain and Poe (1998). This has been validated against the theoretical model of Coppo *et al.* (1996) (see Figure 1, taken from English *et. al.* 2003). The wind direction sensitivity model is based on measurements at 6.8, 10.7, 19.35 and 37 GHz and for a fixed zenith angle of 53 degrees. The original model from St. Germain and Poe (1998) fitted the observational data. Liu and Weng (2003) extended this to predict the sensitivity for an AMSU like instrument (i.e. full range of zenith angle and wider range of frequency).

The relative wind direction is the azimuth line of sight less the wind direction:

$$\phi = \phi_s - \phi_w \qquad (3)$$

The effect of variations in the relative wind direction on the four elements of the Stokes vector (I, Q, U and V) have been shown both theoretically and by experimentation to take the form:

$$\begin{aligned} I &= I_0 + I_1 \cos\phi + I_2 \cos 2\phi \\ Q &= Q_0 + Q_1 \cos\phi + Q_2 \cos 2\phi \\ U &= U_1 \sin\phi + U_2 \sin 2\phi \\ V &= V_1 \sin\phi + V_2 \sin 2\phi \end{aligned} \qquad (4)$$

where I and Q are related to the amplitude and U and V to the phase of the signal. In the Weng model cos(3Φ) and sin(3Φ) are added so the full set of equations are

$$\begin{aligned} I &= I_0 + I_1 \cos\phi + I_2 \cos 2\phi + I_3 \cos 3\phi \\ Q &= Q_0 + Q_1 \cos\phi + Q_2 \cos 2\phi + Q_3 \cos 3\phi \\ U &= U_1 \sin\phi + U_2 \sin 2\phi + U_3 \sin 3\phi \\ V &= V_1 \sin\phi + V_2 \sin 2\phi + V_3 \sin 3\phi \end{aligned} \qquad (5)$$

Note we have assumed the 3rd and 4th element to be zero in the absence of any azimuthal variation. The model has a set of coefficients for calculated I_1, I_2 etc. as a function of wind speed. Note the coefficients are computed to the third power of the wind speed. First these are computed for the original "observed" frequencies of 6.8, 10.7, 19.35 and 37 GHz (i.e. 4 frequencies). So the code has a set of equations for I_1, I_2 etc. as a function of wind speed, W, as follows,

$$I_1 = I_{10} + I_{11} W + I_{12} W^2 + I_{13} W^3 \qquad (6)$$

The Weng model then allows for the zenith angle variation of the "correction" to the emissivity for azimuthal variation by multiplying by (1.0-μ)/(1.0 - 0.6018) where μ = cos(θ) and θ = zenith angle. Thus at the original observation angle of 53 degrees the correction = 1. At nadir the correction = 0. So this correction term simply scales the correction with the viewing angle.

The code then linearly interpolates in frequency. For frequencies above 37 GHz the value at 37 GHz is taken. This is probably an overestimate. For frequencies below 6.8 GHz the 6.8 GHz value is taken, again probably an overestimate.

The RTTOV-8 code has been developed to allow either FASTEM-2 or FASTEM-3 to be invoked according to the coefficient file provided. FASTEM-1 is no longer supported but if a RTTOV-7/FASTEM-2 coefficient file is used and the emissivity input is set to zero the FASTEM-1 values are still computed. For FASTEM-2 the input emissivity must be set to -1.0.

2.3 Improvements to computation of multi-layer cloudy radiances

RTTOV-7 was modified to allow cloud absorption to be taken into account based on the ECMWF broad-band radiation scheme (Morcrette, 1991). Clouds were assumed to be grey bodies with their contribution to the radiances computed from their horizontal

coverage n^i, and their emissivity ε_ν^i in each vertical layer i of the user's model. ε_ν^i is derived from the cloud liquid and/or ice water path l^i by the relationship:

$$\varepsilon_\nu^i = 1 - e^{-l^i k_\nu^i} \qquad (7)$$

where k_ν^i is the extinction coefficient at frequency ν. For RTTOV-8 specific extinction coefficients and single-scattering co-albedos for water clouds are now calculated using constants tabulated in Hu and Stamnes (1993), and specific absorption coefficients are derived from these. The correct viewing angle dependence is also now accounted for. For the diagnosis of water cloud effective radius, the existing logic has been retained, whereby a value of 10 µm is used over land, and 13 µm over sea.

For ice clouds, the absorption coefficient can be computed for either hexagonal column crystals or aggregate crystals. The coefficients for these have been derived from the techniques described in Baran and Francis (2004). The "generalized effective diameter" D_{ge} (Fu, 1996) has been used as the effective size parameter throughout, as this definition is now the most widely-used in the literature. Absorption coefficients at the required wavenumbers are now interpolated rather than sampled, resulting in a more smoothly-varying quantity. There are now four options for diagnosing the effective diameter. The first is based on the Ou and Liou (1995) paper, using just the temperature to predict D_{ge}, and is retained in order to keep some degree of consistency with RTTOV-7 (although some of the existing coding had to be changed to ensure that the definition of effective diameter is treated in a consistent manner - see McFarquhar *et al.* 2003 for a discussion on this subject). Option 2 is based on the Wyser (1998) scheme (using both temperature and ice water content), and option 3 is based on the Boudala *et al.* (2002) scheme (also using both temperature and ice water content). The final option is based on the recent McFarquhar (2003) scheme for tropical cirrus clouds, and depends on ice water content only. The different options are invoked by setting *cld_profiles(j) % kice* and *cld_profiles(j) % kradip* (see Table 5 in users manual).

2.4 Refinements in Line-by-Line transmittance database for coefficient generation

The RTTOV-7 coefficient files are based on the same line-by-line (LbL) model transmittances as used for RTTOV-5/6 which are GENLN2/HITRAN-96 for the infrared and the MPM-89/92 line-by-line calculations (Liebe, 1989) for the microwave. To update the spectroscopic parameters for RTTOV-8 GENLN2 has been rerun in the infrared on a new set of 52 diverse profiles using more up to date spectroscopy from HITRAN-2000 (Rayer 2004). Corresponding reruns using MPM have also been done in the microwave. In addition the water vapour continuum absorption has been computed separately as another variable gas using the CKD2.4 water vapour continuum (Clough S.A. *et. al.* 1989). In addition the kCarta code (Strow *et. al.* 1998) has also been run on the same 52 profiles for use as an alternative to GENLN2 although over a more restricted spectral range. The latter is expected to provide better simulations for AIRS and IASI due to the improvements in CO_2 line mixing. All newly generated coefficient files will use these new transmittance datasets.

2.5 Microwave scattering code for RTTOV-8

To allow simulations of rain affected microwave radiances a scattering code has been provided as part of the RTTOV-8 package in a similar form to that used for simulating cloud affected radiances using rttov_cld. A summary of the scientific contents of *RTTOVSCATT* is given here. Details and original references of model development and evaluation are contained in Bauer (2002), Moreau et al. (2002) and Chevallier and Bauer (2003).

2.5.1 Eddington approximation to microwave radiative transfer

The radiative transfer equation can be expressed as the differential change of radiance L at frequency ν along the propagation path through the atmosphere. In vertical coordinates and including slant paths the vertical coordinate is optical depth $d\delta = k\,dz/\mu$ with zenith angle $\theta = cos^{-1}\mu$ and altitude z. The volume extinction coefficient k is composed of scattering, k_{sct}, and absorption, k_{abs}, contributions, i.e. $k = k_{sct} + k_{abs}$. With the inclusion of source terms and assuming the dependence of radiances on azimuth angle can be neglected, the differential change of L with altitude is:

$$\mu \frac{dL(z;\mu)}{k\,dz} = L(z;\mu) - J(z;\mu) \quad (upward), \tag{8}$$

$$-\mu \frac{dL(z;-\mu)}{k\,dz} = L(z;-\mu) - J(z;-\mu) \quad (downward)$$

The source term, J, covers contributions from scattering (hydrometeors) and emission (oxygen, water vapour, dry air, hydrometeors):

$$J(z;\mu) = \frac{\omega_o}{2}\int_{-1}^{1} L(z;\mu')P(\mu;\mu')d\mu' + (1-\omega_o)B[T(z)] \tag{9}$$

$\omega_o = k_{sct}/k$ denotes the single scattering albedo and provides a measure for the fraction of scattered radiation while $(1-\omega_o)$ is the fraction of absorbed radiation. $B[T(z)]$ is the blackbody equivalent radiance according to temperature T at altitude z. Scattering of radiance is expressed in terms of a normalized scattering phase function:

$$\int_{-1}^{1} P(\mu;\mu')d\mu' = 1 \tag{10}$$

describing the distribution of incident radiance (μ') to observation direction (μ). It can be shown (see Bauer 2002) that

$$P(\mu,\mu') = \frac{1}{2\pi}\int_{0}^{2\pi} P(\mu,\phi,\mu',\phi')d\phi' \tag{11}$$

where ϕ is the azimuth angle.

The Eddington approximation to radiative transfer represents an example of an approximate method. The approximation lies in the development of the radiance vector and phase function to the first order so that only one angle (i.e. the observation angle) is needed and the anisotropic radiance field is decomposed into an isotropic and anisotropic component, respectively:

$$L(z,\mu) = L_o(z) + \mu L_1(z) \qquad (12)$$
$$P(cos\Theta) = 1 + 3\,g cos\Theta$$

with asymmetry parameter g and local scattering angle Θ:

$$\cos\Theta = +\mu\mu' + (1-\mu^2)^{1/2}(1-\mu'^2)^{1/2}\cos(\phi-\phi') \qquad (13)$$

If this expression is substituted first into Eq.12 and then into the expression for $P(\mu,\mu')$ (Eq.11) , and it is assumed that there is no variation with azimuth angle, then

$$P(\mu,\mu') = 1 + 3g\mu\mu' \qquad (14)$$

Then, the source function translates to:

$$J(z,\mu) = [1-\omega_o(z)]B[T(z)] + \omega_o(z)[L_o(z) + g(z)\mu L_1(z)] \qquad (15)$$

for azimuthally averaged fields.

Two mixed equations can be obtained by inserting the expressions for J (Eq. 15) and L (Eq. 12) into Eq. 8. To derive the first equation, take the integral from -1 to 1 w.r.t $d\mu$; for the second equation multiply Eq. 8 by μ and integrate again:

(16)

$$\frac{dL_1(z)}{dz} = -3k(z)\left[1-\omega_o(z)\right]\left\{L_o(z) - B[T(z)]\right\}$$
$$\frac{dL_o(z)}{dz} = -k(z)\left[1-\omega_o(z)g(z)\right]L_1(z)$$

If z' is the height within a layer and assuming that k , ω_0 and g do not vary within an individual layer, their derivatives with respect to z' can be neglected and the second derivative of e.g. L_o provides:

$$\frac{d^2L_o(z')}{dz'^2} = \Lambda^2\left\{L_o(z') - B[T(z')]\right\} \qquad (17)$$

$$\Lambda^2 = 3k^2\left[1-\omega_o\right]\left[1-\omega_o g\right] \qquad (18)$$

For an individual atmospheric layer, the general solution is:

$$L_o(z') = D^+\, exp(\Lambda z') + D^- exp(-\Lambda z') + B[T_o] + B_1(z'-z'_o) \qquad (19)$$

A linear dependence of temperature with optical depth is assumed in the layer, i.e. $B(T) = B(T_o) + B_1(z'-z'_0)$ with lapse rate B_1, temperature at the bottom layer limit, T_o, and layer depth $z'-z'_0$ where z'_0 is the layer bottom.

The coefficients $D^{\pm}$ have to be computed for all layers from the respective boundary conditions, i.e., assumptions made at the Earth's surface and the top of the atmosphere,

as well as from the requirement of flux continuity at the layer interfaces. At any point, the total upward flux density, F^+ , can be written as

$$\begin{aligned} F^+ &= \int_{-1}^{1} \mu L(z,\mu) d\mu \\ &= \int_{0}^{1} (L_0(z) + \mu L_1(z)) \mu d\mu \\ &= L_0(z) + \frac{2}{3} L_1(z) \end{aligned} \tag{20}$$

Similarly, the downward flux density is $F^- = L_0(z) - \frac{2}{3} L_1(z)$ (21)

From the second part of Eq. 16, and writing $h = \frac{3}{2} k(1-\omega_0 g)$, the upward and downward flux densities at any point can be written as

$$\begin{aligned} F^+ &= \left(L_o + \frac{\partial L_o}{h \partial z} \right) \\ F^- &= \left(L_o - \frac{\partial L_o}{h \partial z} \right) \end{aligned} \tag{22}$$

A lower threshold value of *h* is enforced to avoid division by zero; very small values of *h* are set to 10^{-5} Np/km. Applying assumptions about cold space radiation at the top of the atmosphere ($z = z^*$), polarized (*p*) surface emission and reflection at the bottom of the atmosphere ($z = z_0 = 0$) and flux continuity at layer boundaries, the following equations are derived:

$$\begin{aligned} \left(L_o - \frac{\partial L_o}{h \partial z'} \right)_{z=z^*} &= B(2.7) \\ \left(L_o + \frac{\partial L_o}{h \partial z'} \right)_{z=0} &= \bar{\varepsilon}_p B(T) + (1-\bar{\varepsilon}_p) \left(L_o - \frac{\partial L_o}{h \partial z'} \right)_{z=0} \\ \left(L_o \pm \frac{\partial L_o}{h \partial z'} \right)_{z=z_i}^{i} &= \left(L_o \mp \frac{\partial L_o}{h \partial z'} \right)_{z=z_i}^{i+1} \end{aligned} \tag{23}$$

The terms in brackets denote the downward (-) and upward (+) directed flux densities, $h = 1.5k(1-\omega_o g)$ and $z = z_i$ denotes the i-th layer interface between i-th and (i+1)-th layer. Since the continuity requirement applies to flux densities, the polarized hemispheric emissivity, ε_p, is used which is calculated from the integration of the specular emissivity over the hemisphere:

$$\bar{\varepsilon}_p = 2 \int_0^1 \varepsilon_p(\mu) \mu d\mu \tag{24}$$

This integration is carried out within the FASTEM routines and so does not have to be repeated with the RTTOVSCATT code.

2.5.2 Implementation

A system of linear equations of the form $AD^{\pm} = B$ can be formulated from inserting Eq. 19 into Eqs. 23. For N atmospheric layers, this system contains $2(N-2)$ equations for the layer interfaces as well as one at the top and bottom of the atmosphere, respectively. Therefore, A is a $(2N \times 2N)$-matrix and B is a $(2N)$-vector with elements a_{mn} and b_m, respectively. For each layer, i, $j = 2i$:

$$\begin{aligned} a_{j,j-1} &= L_i^+ exp[\Lambda_i \Delta z_i] \\ a_{j,j} &= L_i^- exp[-\Lambda_i \Delta z_i] \\ a_{j,j+1} &= -L_i^+ \\ a_{j,j+2} &= -L_i^- \\ b_j &= C_j - C_i \end{aligned} \tag{25}$$

$$\begin{aligned} a_{j+1,j-1} &= L_i^- exp[\Lambda_i \Delta z_i] \\ a_{j+1,j} &= L_i^+ exp[-\Lambda_i \Delta z_i] \\ a_{j+1,j+1} &= -L_i^- \\ a_{j+1,j+2} &= -L_i^+ \\ b_{j+1} &= C_i - C_j \end{aligned} \tag{26}$$

and for the top and bottom layers:

$$\begin{aligned} a_{1,1} &= L_1^- - \overline{\rho}_p L_1^+ \\ a_{1,2} &= L_1^+ - \overline{\rho}_p L_1^- \\ b_1 &= B(T_s)(\overline{\varepsilon}_p + \overline{\rho}_p - 1) + C_1(\overline{\rho}_p + 1) \end{aligned} \tag{27}$$

$$\begin{aligned} a_{2N,2N-1} &= L_N^+ exp[\Lambda_N \Delta z_N] \\ a_{2N,2N} &= L_N^- exp[-\Lambda_N \Delta z_N] \\ b_{2N} &= B(T_{sp}) - B(T_{N-1}) - C_N \end{aligned} \tag{28}$$

with $C_i = B_{1i}/h_i$, $L_i^{\pm} = 1 \pm \Lambda_i/h_i$, $\overline{\rho}_p = 1 - \overline{\varepsilon}_p$, and $h_i = 1.5 k_i (1 - \omega_{o,i} g_i)$. $B(T_s)$ denotes radiance emitted by the surface with skin temperature, $B(T_{sp})$ corresponds to radiation of space (assumed to be 2.7K), B_{1i} is the i-th layer's lapse rate and $B(T_{n-1})$ the radiance according to temperature at the interface between layers N and $N-1$. The equations above are computed in the subroutine *rttov_boundaryconditions.* Once $D^{\pm}$ have been obtained, they can be used in the integration of the source function (Eq. 15).

The source term from Eq. 15 has to be integrated for each layer between $z' = 0$ and $z' = \Delta z_i$. This is performed in *rttov_integratesource* for up/downwelling radiances respectively

$$J_i^+ = J_{a,i}^+ aa_i + J_{b,i}^+ bb_i + J_{c,i}^+ cc_i + J_{d,i}^+ dd_i$$
$$J_i^- = J_{a,i}^- aa_i + J_{b,i}^- bb_i + J_{c,i}^- cc_i + J_{d,i}^- dd_i \quad (29)$$

with:

$$aa_i = B_{0i} - \frac{3g_i\omega_{o,i}\mu B_{1i}}{2h_i}$$
$$bb_i = B_{1i} \quad (30)$$
$$cc_i = D_i^+\omega_{oi}(1 - \frac{g_i\mu\Lambda_i}{2h_i})$$
$$dd_i = D_i^-\omega_{oi}(1 + \frac{g_i\mu\Lambda_i}{2h_i})$$

and partial source terms:

$$J_{ai}^+ = 1 - \tau_i \quad (31)$$
$$J_{bi}^+ = \Delta z_i - \frac{\mu(1-\tau_i)}{k_i}$$
$$J_{ci}^+ = \frac{k_i}{k_i + \Lambda_i\mu}[exp(\Delta z_i\Lambda_i) - \tau_i]$$
$$J_{di}^+ = \frac{k_i}{k_i - \Lambda_i\mu}[exp(-\Delta z_i\Lambda_i) - \tau_i]$$
$$J_{ai}^- = 1 - \tau_i \quad (32)$$
$$J_{bi}^- = \frac{\mu}{k_i}(1-\tau_i) - \tau_i\Delta z_i$$
$$J_{ci}^- = \frac{k_i}{\Lambda_i\mu - k_i}\{exp[\Delta z_i(\Lambda_i - k_i/\mu)] - 1\}$$
$$J_{di}^- = \frac{k_i}{\Lambda_i\mu + k_i}\{1 - exp[-\Delta z_i(k_i + \Lambda_i\mu)/\mu]\}$$

Radiance B_{0i} corresponds to the temperature at the bottom interface of layer i and τ_i is the layer transmittance, $\tau_i = exp(k_i\Delta z_i/\mu)$. The partial source terms in Eq. 31 and Eq. 32 are calculated only if the single scattering albedo is above a certain threshold (which is determined by the Mie tables); otherwise they are set to equal zero. Finally, the integration of contributions from each layer through the atmosphere is carried out, first downward then upward:

$$L_i^- = L_{i+1}^-\tau_i + J_i^- \quad (33)$$
$$L_i^+ = L_{i-1}^+\tau_i + J_i^+$$

with:

$$L_{N+1}^{-} = B(2.7) \qquad (34)$$
$$L_0^{+} = B(T_s)\varepsilon_p + (1-\varepsilon_p)L_1^{-}$$

in *rttov_eddington*, ε_p is the polarized surface emissivity thus L_0^{+} has to be calculated for each polarization.

2.5.3 Optical properties

The background (i.e. clear-sky) absorption contribution as well as surface reflection and emission are calculated with the RTTOV-8 routines *rttov_transmit* and *rttov_calcemis_mw*. The optical properties of hydrometeors are stored in sensor specific coefficient files. Details of the underlying assumptions on particle permittivity as a function of frequency and temperature, size distribution as a function of hydrometeor type and water/ice content, particle density as a function of hydrometeor type can be found in Bauer (2001).

The files contain tables of hydrometeor optical properties that are calculated for the relevant frequencies, environmental temperatures, and hydrometeor contents. Only extinction coefficient, single scattering albedo, and asymmetry parameter that were integrated over the particle size spectra ($N(D)$ with particle diameter D) are required to perform the radiative transfer calculations. These have to be integrated over the size spectrum for each hydrometeor type:

$$k, \omega_o, g = \frac{\pi}{4}\int_0^{\infty}\left[Q, \frac{Q_{sct}}{Q}, \frac{\overline{cos\theta}}{Q_{sct}}\right](D)N(D)D^2 dD \qquad (35)$$

with scattering and extinction cross sections Q_{sct} and Q, average scattering angle $\overline{cos\theta}$ at frequency ν and temperature T. The cross sections Q are obtained from Mie-calculations assuming spherical particle shape for all hydrometeor types.
The contributions from co-existing hydrometeor types are integrated for each layer i by:

$$k_i = \sum_j k_{i,j}, \quad j = r, s, g, h, w, i$$
$$\omega_{o,i} = \frac{\sum_j \omega_{o,i,j}\, k_{i,j}}{\sum_j k_{i,j}}$$
$$g_i = \frac{\sum_j g_{i,j}\, \omega_{o,i,j}\, k_{i,j}}{\sum_j \omega_{o,i,j}\, k_{i,j}} \qquad (36)$$

Indices $j = r, s, g, h, w, i$ refer to rain, snow, graupel, hail, cloud liquid water and cloud ice, respectively.
The tables use the following discretisation in hydrometeor types j, frequency n, temperature l, liquid water / ice content m:

- 6 hydrometeor types, $j \in [1..6]$ for rain, snow, graupel, hail, cloud liquid water and cloud ice. For details on assumptions for size distributions and densities refer to Bauer (2001).
- As many frequencies as covered by the specific microwave radiometer and assuming monochromatic centre frequencies, i.e., negligible bandwidths, e.g., for the SSM/I: $n \in [1..4]$ for 19.35, 22.235, 37.0, and 85.5 GHz.
- 70 temperature indices: for liquid particles $l = T_i - 233\,K$ thus $T_i \in [234, 303\,K]$, for frozen particles $l = T_i - 203\,K$ thus $T_i \in [204, 273\,K]$.
- 401 liquid/ice water content indices: $m = 100 \cdot log_{10}(w_{i,j})$ thus $w_{i,j} \in [0.001, 10\,g\,m^{-3}]$ with hydrometeor type index j and layer index i.

The calculation of the layer optical properties from input water contents and temperature for each frequency and profile are carried out in *rttov_mieproc* using the above index conversion and the summations from Eq. 36.

The Delta-approximation modifies k_i, ω_{oi}, and g_i as a consequence of the approximation of the fractional forward peak of the phase function by a delta-function:

$$g_i' = \frac{g_i}{1+g_i}, \quad \omega_{oi}' = \frac{(1-g_i)^2 \omega_{oi}}{1-g^2 \omega_{oi}}, \quad k_i' = (1-\omega_{oi} g_i^2) k_i \tag{37}$$

which has proven to significantly improve the treatment of radiative transfer in two-stream-type models in strongly scattering media. Therefore, k_i', ω_{oi}', and g_i' replace k_i, ω_{oi}, and g_i where required in all above equations. The layer optical depth becomes $\delta_i' = k_i' \Delta z_i' / \mu$ and layer transmission is $\tau_i' = exp(-\delta_i')$. The optical quantities k_i, ω_{oi}, g_i, h_i, δ_i, τ_i, Λ_i are calculated per layer, per frequency and per profile in *rttov_iniedd*.

3. Testing and Validation of RTTOV-8

To ensure no bugs have entered in the RTTOV code during the introduction of the above changes an extensive set of tests were applied to the new model before it was released. The use of the RTTOV-7 optical depth predictors should give identical results with the new code to the old RTTOV-7 code within machine precision. The new RTTOV-8 optical depth predictors will give different radiances and are validated as described below. The new RTTOV-8 code is validated in several ways:

- The RTTOV-8 top of atmosphere radiances computed using either the old and new optical depth predictors are compared with those computed in the same way as in RTTOV but using the LbL model transmittances from a 117 ECMWF profile independent set (Chevallier, 2000). This tests the accuracy of the brightness temperatures simulated by RTTOV-8 but disregarding errors coming from the LbL model.
- The RTTOV-8 top of atmosphere radiances have been compared with observed ATOVS radiances using NWP analyses to provide the state vector.

- The RTTOV-8 jacobians for both sets of optical depth predictors have been compared for ATOVS channels using the dataset prepared by Garand *et al.* (2001). This allows a comparison with several different models.
- Validation of the fast surface emissivity model FASTEM-3 with Windsat data
- Validation of the new treatment of cloud in RTTOV_CLD
- Validation of the new RTTOVSCATT simulations

There was also an extensive series of comparisons carried out, not described here, between RTTOV-7 and RTTOV-8 transmittances, radiances, jacobians and surface emissivities from the direct, TL, AD and K codes to check there are no differences during the code development except those anticipated. The tests conducted are in the RTTOV-8 test plan document and users can run these tests to verify the performance of the code on their platform.

Comparisons can be made with several different sets of profiles with pre-computed LbL transmittances. A set of 43 profiles (42 TIGR/HALOE measured temperature and water vapour profiles plus mean) and 34 NESDIS ozone profiles described in Matricardi and Saunders (1999) were used to generate the transmittance model coefficients for mixed gases, water vapour and ozone. This is the dependent set. Secondly an independent set of 117 profiles picked from the 50 level ECMWF analyses (Chevallier, 2000) with varying temperature and water vapour from the analyses and ozone from a latitude dependent climatology (Fortuin and Langematz, 1994) was used. Note profiles with surface pressures less than 950 hPa were not included in either sets. Thirdly the 52 profile dataset are a diverse set of model profiles picked from the 60 level ECMWF model profile where ozone is an analysed variable. This profile set is the new dependent set for the latest GENLN2 and kCarta transmittances.

The validation results described below are mainly for ATOVS, SEVIRI and AIRS but the performance of the model for all new instruments is checked in terms of transmittance differences from the LbL model and compared to similar channels in the above sensors.

3.1 Validation of top of atmosphere radiances

The primary output from RTTOV is the top of atmosphere radiance for each channel and so this is the main parameter by which RTTOV-8 is validated. The radiances are compared with radiances computed from the LbL model used to produce the dependent set transmittances and with radiances computed from other LbL models. In addition they are also compared with observations using NWP model profiles as an input to RTTOV.

3.1.1 Comparison with independent dataset of line-by-line computed transmittances

This comparison determines the accuracy of the regression scheme itself since the *same* LbL models were used to generate the RTTOV coefficients. For both the

dependent set and independent profile sets brightness temperatures have been computed using the radiative transfer layer integration within RTTOV-8 to ensure any differences are only due to the LbL and fast model transmittances not the integration of the radiative transfer through the atmosphere. For the RTTOV-7 predictors no changes from RTTOV-7 to RTTOV-8 code were expected and so to verify this comparisons were made with the 117 independent profile set for ATOVS and SEVIRI for the RTTOV-7 and RTTOV-8 codes.

Figures 2 and Tables 5, 6 and 7 document the comparison between the RTTOV-8 fast model and line-by-line model brightness temperatures for the 117 independent profile set for NOAA-15 ATOVS over five zenith angles in the range 0-60 deg. In this case the line-by-line models were GENLN2 for the infrared and Liebe for the microwave. The figures shows the bias and standard deviations of the RTTOV-LBL differences are very similar for both models as expected giving confidence that the recoding has not introduced any errors. The mean biases for the two versions of the model are all less than 0.2K.

Equivalent plots for the MSG-1 SEVIRI channels are given in Figures 3 and Table 8. Note that in contrast to the ATOVS plots these are for 6 zenith angles out to 63.6 deg as these geostationary imager radiances can measure at angles beyond 70 deg towards the edge of the Earth's disk as seen from geostationary orbit.

For the accuracy of radiances from other sensors results from similar channels on sensors documented above can be used. For example for AVHRR and other geostationary imagers one can use the MSG-1 SEVIRI values as a guide for the equivalent channels. Also the extended set of results in R7REP2002 can also be used as being representative for the RTTOV-8 model with the RTTOV-7 predictors invoked.

For the new set of predictors defined in Tables 2 and 3 a new set of GENLN2 and kCarta line-by-line transmittances for the 52 diverse ECMWF model profiles at 43 levels and 101 levels were computed as a new dependent sets. In this case water vapour transmittances are separated out into line absorption and continuum absorption in contrast to the earlier GENLN2 transmittances. Figure 4 compares the RTTOV-7 optical depth predictors with RTTOV-8 optical depth predictors for the 52 profile dependent set. Coefficients were derived for both 43 levels (to match the old datasets) and on a new set of 101 AIRS pressure levels defined on the RTTOV web page at http://www.metoffice.com/research/interproj/nwpsaf/rtm/diverse_52profiles_101L.dat. In addition CO_2 was optionally made a variable gas with its own set of optical depth predictors. In terms of bias the RTTOV-8 predictors generally have the same or lower bias but differences are all at the 0.01K level. The move to 101 levels has little effect on the biases. When variable CO_2 is included on 101 levels the biases are unchanged for most channels except HIRS channels 4-6 where there is a small increase in the bias. In terms of standard deviation of the differences the change of predictors has only a small effect but increasing the number of levels from 43L to 101L does reduce the standard deviation by up to 50% for some of the water vapour channels. The standard deviation increases for variable CO_2 for HIRS channels 4-7.

Comparisons with kCarta line-by-line brightness temperatures for AIRS have also been made as shown in Figures 5 and 6. Figure 5 is a direct comparison of RTTOV-7

optical depth predictors with RTTOV-8 optical depth predictors (separate water vapour line and continuum) on 43 levels for 52 diverse profiles from the ECMWF model for all the AIRS channels. A small increase in the mean bias and standard deviation with kCarta is noted for RTTOV-8 predictors in some of the very strong water vapour lines but for most channels the bias/variance is the same for both models. Note for this plot the integration over levels of the radiances is identical and only the level to space transmittances are different, from RTTOV and from kCarta. For Figure 6 the effect of increasing the number of levels on the accuracy of the radiative transfer calculation is demonstrated for AIRS by comparing a 43L computation with a 101L computation. The maximum biases and standard deviations reduce from 0.5K to 0.2K for all the AIRS channels except for those in the water vapour band which show only small benefits in the increased vertical resolution of the RTTOV calculations. In terms of standard deviations of the differences most channels are improved except for the ozone and strong water vapour lines. Applying the variable CO_2 predictors to the AIRS channel simulations showed negligible differences with assuming CO_2 is a mixed gas as shown in Figure 7.

3.1.2 Comparison with other radiative transfer model computed radiances

The results described above in section 3.1.1 all compare the radiances with radiances computed using the same LbL model from which the RTTOV coefficients were generated. Hence errors in the LbL models themselves (i.e. GENLN2/MPM) are not included in the above estimates. In R7REP2002 several infrared models were used to compare with various RTTOV simulations and for the RTTOV-7 optical depth predictors these comparisons are still valid for the RTTOV-8 code. However more recent comparisons have been carried out and Table 9 documents a comparison between RFM (a version of GENLN2) for several different RT models including RTTOV-7 with ordinary and Plank weighted coefficients for the SEVIRI infrared channels (Merchant, 2003). The results in the table show the significant reduction in the RTTOV-7 bias for the SEVIRI 3.9μm channel when the Planck weighted coefficients are used (see 2.1). For the other three SEVIRI channels the biases are all less than 0.1K with respect to RFM (the same family of models on which RTTOV is based) but up to 0.6K biases are seen when compared to MODTRAN and RAD7 for the SEVIRI 8.7μm channel. For the 11 and 12 μm channels the differences are <0.2K.

In the microwave region there are less independent LbL models to compare with. The most comprehensive recent comparison which included RTTOV-6 simulations was the Garand *et. al.* (2001) intercomparison. RTTOV-8 is based on the same LbL model as RTTOV-6 so the results from Garand *et. al.* (2001) can still be applied to RTTOV-8. The results from Garand *et. al.* (2001) are reproduced here as Table 10 and there are no changes from RTTOV-7.

3.1.3 Comparison with observations

Another validation of the simulated radiances is to compare with real observations. A comparison of NOAA-16 ATOVS radiances with simulated radiances using ECMWF NWP model fields and RTTOV-7 and RTTOV-8 is plotted in Figure 8. The top panel shows the mean bias for 21 days in March 2004 and the bottom panel the standard deviation of the observed minus model differences. There are a few small differences

in the bias (few tenths of degK) which can be explained by differences in the numbers of each sample due to subtle changes in q/c applied for the different model. The differences in standard deviation are all negligible.

3.2 Validation of jacobians

The accuracy of the jacobians computed by RTTOV are important to document for the radiance assimilation users as they are instrumental in modifying the NWP model analysis variables. This section describes a validation of the jacobians generated by RTTOV-8 by comparing them with other line-by-line and fast RT models for AIRS and AMSU.

3.2.1 AIRS comparisons

A diverse profile dataset was used to compute for a few key AIRS channels the nadir view jacobians for temperature, water vapour and ozone. Computations were made by RTTOV-7, RTTOV-8 and RFM (i.e. a version of GENLN2 a line-by-line model using HITRAN-2000) and the latter jacobians were used as a reference dataset which the RTTOV values are compared with. The prescribed temperature perturbation was +1K, and for water vapour and ozone it was -1% of the layer mean concentration. Note that the RTTOV-7 values were computed on the standard 43 pressure levels and then transformed to 101 levels using the adjoint of the interpolation routine to enable comparisons to be made. The "Garand measure of fit" was used to summarise how well each version of RTTOV fitted the RFM jacobians as defined by *M*:

$$M = 100 \times \sqrt{\frac{\sum \left(X_i - X_{ref} \right)^2}{\sum \left(X_{ref} \right)^2}} \tag{38}$$

Unfortunately neither version of RTTOV was based on the RFM transmittances so some of the misfits are due to forward model differences from the different line databases used. RTTOV-7 results are based on GENLN2/HITRAN-96 and RTTOV-8 results are based on kCarta/HITRAN2004. Table 11 lists the 20 AIRS channels which were selected for the jacobian comparisons.

The results are summarised in Figure 9 where RTTOV-7 and 8 are compared with RFM jacobians for all 52 diverse profiles. For the temperature jacobians the RTTOV-8 fit is generally the same or closer to RFM except for AIRS channels 2107 (2386 cm^{-1}) and 2197 (2500 cm^{-1}) where the RFM model transmittances are significantly different from the kCarta transmittances used by RTTOV-8 which causes differences in the jacobians also. Figure 10 illustrates this where for a particular profile the sensitivity of the channel to changes in near surface temperatures is much higher for RTTOV-8. For the water vapour jacobians RTTOV-8 is clearly doing better than RTTOV-7 for AIRS channels 672 (871 cm^{-1}) and 1142 (1074 cm^{-1}). The reason appears to be the behaviour of both versions of RTTOV for cold dry profiles which is not optimal for either model (see bottom left hand panel in Figure 10) but on average RTTOV-8 is more stable than RTTOV-7. Note as these are dry profiles the absolute values of the Jacobians are small and so the effect on retrievals may be small. The better vertical resolution for 101L

RTTOV-8 over 43L RTTOV-7 is also shown in the bottom right hand plot of Figure 10. For ozone jacobians RTTOV-8 fits RFM closer than RTTOV-7 for the two ozone channels selected.

A more comprehensive comparison of RTTOV-7 and RTTOV-8 AIRS simulations with other line-by-line and fast models has been carried out and the results will soon be published which will be a further validation of the RTTOV models.

3.2.2 AMSU comparisons

Several users have reported unphysical spikes with AMSU-A water vapour jacobians for RTTOV-7 which made the convergence in variational assimilation more difficult. A comparison was therefore made between AMSU-A jacobians computed using RTTOV-7 and RTTOV-8 predictors to see if these spikes are reduced in RTTOV-8. The 117 ECMWF profile set was used to compute the jacobians as they are independent from the profile sets used to generate the coefficients. Figure 11 shows for one profile water vapour jacobians for the 15 AMSU-A channels and shows that the RTTOV-7 jacobians 11(a) have many spikes compared with the RTTOV-8 jacobians 11(b) which are much smoother. The levels affected are mainly in the stratosphere but can have tails which penetrate down to the tropopause. The same is true for other profiles. It is planned to compute the corresponding jacobians from the microwave line by line model to check that the RTTOV-8 jacobians are also closer to the 'truth'.

3.3 Validation of surface emissivity models

There have been no changes to the infrared sea surface emissivity model since RTTOV-6/7 and so the results in Sherlock (1999) are still valid.

For the microwave the ocean surface model FASTEM-2 was upgraded to FASTEM-3 as described in section 2.2 above. The new model has been tested by comparing simulated Windsat radiances from the Met Office model fields with observed Windsat radiances. Figure 12 shows an improved fit for all channels (except 37GHz circular polarisation which is broken) for 2 wind speed regimes. Improvements of up to 30% over FASTEM-2 are obtained for some channels. FASTEM-3 is still biased at frequencies below 10GHz (Windsat and AMSR both show this) because the current treatment of the sea surface roughness is unphysical at these low frequencies.

3.4 Infrared cloudy radiance simulations

The RTTOV-8 model includes a set of routines to simulate cloudy radiances. These have been improved since RTTOV-7 as described above in section 2.3. Some comparisons have been made with the RTTOV-7 and 8 cloudy simulations. Figure 13 shows for the liquid water profile in panel (a) the different absorption coefficients for (b) HIRS channels 8 (11.1μm) and (c) 18 (3.8μm). The differences in terms of brightness temperature of the HIRS channels are shown in panel (d) and can be up to 0.5degK for the shortwave channels. A similar plot for ice cloud is shown in Figure 14 where the ice water content assumed is shown in panel (a) and the ice crystal effective diameter in panel (b). RTTOV-7 did not allow the absorption coefficient to be a function of ice crystal habits but as shown in panel (c) this is possible for RTTOV-8.

Panel (d) shows the brightness temperature differences between RTTOV-7 and 8 for HIRS channels 7 (13.3μm), 8 (11.1μm) and 11 (7.33 μm) which for HIRS channel 8 can be up to 5degK according to the different schemes for diagnosing the ice crystal effective diameter. It is hoped these improved parameterisations will lead to more accurate simulations of cloudy radiances. The comparisons of the new RTTOVCLD simulations with observations have not yet been done to assess this however.

3.5 Microwave scattering radiance simulations

Qualitative comparisons have been made between RTOVSCATT simulations and AMSU-A radiance observations over NW Europe. Figure 15 shows comparisons for a case study at 13Z on 25 January 2002. Data from the Met Office Mesoscale Model was used to create input profiles for RTTOVSCATT and simulations were run with RTTOV-8 and RTTOVSCATT and the output brightness temperatures compared to NOAA-16 observations. Figure 15a shows the observed NOAA-16 brightness temperatures over the UK area for AMSU-A window channels 1, 2, 3 and 15 (23.8GHz, 31.4GHz, 50.3GHz and 89.0GHz respectively). Figure 15b shows the corresponding simulated brightness temperatures obtained using RTTOVSCATT with input profiles of rain, snow, ice and liquid water. Figure 15c is the corresponding output from the RTTOV-8 run with no scattering (but including emission effects from liquid water). Figure 15d is the corresponding output from RTTOV-8 simulations where both scattering effects and the emissions effects from liquid water have been neglected (i.e. a clear air simulation).

It can be seen from Figures 15c and 15d that modelling the emission signal of liquid water has a large effect on all the window channels, as would be expected at these frequencies where sensitivity to liquid water emission is high. Including the effects of scattering from atmospheric hydrometeors (Figure 15b) again brings the simulations closer to the observed brightness temperatures (15a) . For the window channels at the lower frequencies (23.8 and 31.4GHz), microwave radiation will pass through clouds and will interact with precipitation beneath. At the higher frequencies, scattering from ice particles becomes important. The plots demonstrate that RTTOVSCATT is able to simulate the amplitude of the signals seen in observations in cloudy and precipitating areas to a qualitatively better extent than the RTTOV non-scattering code for the AMSU-A window channels.

The RTTOVSCATT code has been integrated within the operational IFS code at ECMWF which has allowed global comparisons between SSM/I precipitation affected radiances and RTTOVSCATT simulations. Figure 16 shows observed minus first guess departures for all the SSM/I channels for precipitation affected areas compared to those for clear skies with clear sky RTTOV-8 simulations. Although the differences for precipitation affected radiances do have a broader distribution it is encouraging they are at least similar and Gaussian in distribution.

It is early days for the assimilation of precipitation affected microwave radiances but RTTOVSCATT looks as if it will be able to provide the first step in understanding the observed minus model differences in microwave radiance space.

4. Summary and Future Developments

The latest version of RTTOV, RTTOV-8 has been validated in several ways to show the same or improved performance for the prediction of satellite top of atmosphere radiances both for clear air, cloudy and precipitating profiles. It builds on previous versions of RTTOV.

For RTTOV-9 due for release in early 2007 the following changes are planned:

- Investigate optical depth predictors to show the relationship between accuracy and number of predictors (i.e. CPU cost) and optimise if possible
- Add reflected solar radiation
- Improve IR land surface emissivity
- Make input profile pressure levels flexible as specified by user
- Extend number of variable gases
- Provide more coefficient files based on new spectroscopic datasets (i.e. GENLN2 and kCarta)
- Add new sensors as required

Users of the code are invited to submit comments for improvements or report bugs to mailto:nwpsaf@metoffice.gov.uk. An RTTOV email newsgroup exists to share experiences, report bugs and broadcast information on updates to the coefficient files or code. Just send a request to this email to be included on the list.

5. Acknowledgements

The RTTOV-8 developments and validation described here were carried out as part of the EUMETSAT funded NWP-SAF activities by the Met Office, ECMWF and MétéoFrance.

6. References

Baran, A.J. & Francis, P.N., 2004: On the radiative properties of cirrus cloud at solar and thermal wavelengths: A test of model consistency using high resolution airborne radiance measurements. *Q. J. Roy. Meteor. Soc.* **130** *763*

Bauer, P., 2001: Including a melting layer in microwave radiative transfer simulation for clouds. *Atmos. Res.*, **67**, *9-30*.

Bauer, P., 2002: Microwave radiative transfer modelling in clouds and precipitation, Part I: Model description. *Satellite Application Facility for Numerical Weather Prediction, NWP-SAF-EC-TR-005*.

Boudala, F.S., Isaac, G.A., Fu, Q. & Cober, S.G., 2002 : Parameterization of effective ice particle size for high-latitude clouds. *Int. J. Climatol.*, **22,** *1267-1284*.

Brunel, P. and S. Turner, 2003: On the use of Planck-weighted transmittances in RTTOV. *Poster at 13tth International TOVS Study Conference, Ste Adéle, Canada, 29 October 2003 - 4 November 2003* *http://cimss.ssec.wisc.edu/itwg/itsc/itsc13/thursday/brunel_poster.pdf*

Chevallier, F. 2000 TIGR-like sampled databases of atmospheric profiles from the ECMWF 50 level forecast model. NWP-SAF report 1. *NWP SAF Report available from* *http://www.ecmwf.int/publications/library/do/references/list/202*

Chevallier, F., and P. Bauer, 2002: Microwave radiative transfer modelling in clouds and precipitation, Part III: Model rain and clouds over oceans – comparison with SSM/I observations. *Satellite Application Facility for Numerical Weather Prediction, NWP-SAF-EC-TR-007.*

Chevallier, F. and P. Bauer, 2003: Model rain and clouds over oceans: Comparison with SSM/I observations. *Monthly Weather Review*, **131**, *1240-1255*.

Coppo P., J.T. Johnson, L. Guerriero, J.A. Kongm, G. Macelloni, F. Marzano, P. Pampaloni, N. Pierdicca, D. Solimini, C. Susini, G. Tofani, Y. Zhang, 1996: Polarimetry for passive remote sensing. *ESA Study report contract number 1146/95/NL/NB.*

Deblonde, G. 2000 Evaluation of FASTEM and FASTEM-2. *NWP SAF Report available from RTTOV web site:* http://www.metoffice.com/research/interproj/nwpsaf/rtm/

Deblonde, G. and S.J. English 2001 Evaluation of the FASTEM-2 fast microwave oceanic surface emissivity model. *Tech. Proc. ITSC-XI Budapest, 20-26 Sept 2000 67-78*

English S. J., A. Jupp, B. Candy, D. Bebbington, A. Holt, 2003: Capability and requirements for polarimetric radiometry in numerical weather prediction for surface wind analysis. *First progress report for ESA contract reference number CAO/CB/02.1025.*

Eyre J.R. and H.M. Woolf 1988 Transmittance of atmospheric gases in the microwave region: a fast model. *Applied Optics* **27** *3244-3249*

Eyre J.R. 1991 A fast radiative transfer model for satellite sounding systems. *ECMWF Research Dept. Tech. Memo.* **176** *(available from the librarian at ECMWF).*

Fortuin, J.P.F and U. Langematz 1994 An update on the global ozone climatology and on concurrent ozone and temperature trends. *Proc. SPIE.* **2311** *207-216.*

Fu, Q., 1996: An accurate parameterization of the solar radiative properties of cirrus clouds., *J. Clim.*, **9,** *2058-2082*.

Garand, L., Turner, D.S., Larocque, M., Bates, J., Boukabara, S., Brunel, P., Chevallier, F., Deblonde, G., Engelen, R., Hollingshead, M., Jackson, D., Jedlovec, G., Joiner, J., Kleespies, T., McKague, D.S., McMillin, L., Moncet, J. L., Pardo, J. R., Rayer, P. J., Salathe, E., Saunders, R., Scott, N. A., Van Delst, P., Woolf, R. 2001 Radiance and jacobian intercomparison of radiative transfer models applied to HIRS and AMSU channels. *J. Geophys. Res.*, **106**, *D20. 24,017-24031.*

Harris, B. and G. Kelly 2001 B. A. Harris and G. Kelly - A satellite radiance-bias correction scheme for data assimilation. *Q. J. Roy. Meteorol. Soc.* **127** *1453*

Hu, Y.X. & Stamnes, K., 1993: An accurate parameterization of the radiative properties of water clouds suitable for use in climate models. *J. Clim.*, **6,** *728-742*.

Liu, Q., and F. Weng, 2003: Retrieval of Sea Surface Wind Vector from Simulated Satellite Microwave Polarimetric Measurements, *Radio Science*, **38**(4) *8078*.

Matricardi, M and Saunders, R.W. 1999 A fast radiative transfer model for simulation of IASI radiances. *Applied Optics*, **38**, *5679-5691*.

Matricardi, M. 2003 RTIASI-4 A new version of the ECMWF fast radiative transfer model for the infrared atmospheric sounding interferometer. *ECMWF Research Dept. Tech. Memo.* **425**.

Matricardi, M., Chevallier F, Kelly G, Thepaut J-N 2004 An improved general fast radiative transfer model for the assimilation of radiance observations. *Q. J. Roy. Meteorol. Soc.* **130** *153-173*

McFarquhar, G.M., Iacobellis, S. & Somerville, R.C.J., 2003 : SCM simulations of tropical ice clouds using observationally based parameterizations of microphysics. *J. Clim.*, **16,** *1643-1664*.

Merchant, C.J. 2003 Comparisons of radiative transfer simulations for seviri (thermal channels). *Ocean and Sea-Ice SAF visiting Scientist Report. July-Oct 2003.*

Morcrette, J.J. 1991 Radiation and cloud radiative properties in the ECMWF forecasting system. *J. Geophys. Res.***96** *D5 9121-9132.*

Moreau, E., P. Bauer, and F. Chevallier, 2002: Microwave radiative transfer modeling in clouds and precipitation. Part II: Model evaluation. *NWP-SAF report No. 6, available from* *http://www.ecmwf.int/publications/library/do/references/list/202*

Ou S.-C. and K.-N. Liou 1995 Ice microphysics and climatic temperature feedback. *Atmos. Res.* **35** *127-138.*

Rayer P.J. 1995 Fast transmittance model for satellite sounding. *Applied Optics*, **34** *7387-7394*.

Rayer, P.J. 2004 RTGEN a shell script for transmittance and radiance calculations. *NWP SAF working paper (copy available from author).*

Rizzi, R. and M. Matricardi 1998 The use of TOVS clear radiances for numerical weather prediction using an updated forward model., *Q. J. Roy. Meteorol. Soc.* **124** *1293-1312*

St. Germain, K., and G. Poe, 1998: Polarimetric emission model of the sea at microwave frequencies, Part II: Comparison with measurements. *Washington, D. C., Naval Research Laboratory Report, 1998.*

Saunders R.W., M. Matricardi and P. Brunel 1999a A fast radiative transfer model for assimilation of satellite radiance observations - RTTOV-5. *ECMWF Research Dept. Tech. Memo.* **282** *(available from* *http://www.ecmwf.int/publications/library/do/references/list/14* *).*

Saunders R.W., M. Matricardi and P. Brunel 1999b An Improved Fast Radiative Transfer Model for Assimilation of Satellite Radiance Observations. *Q. J. Roy. Meteorol. Soc. ,* **125,** *1407-1425*.

Sherlock, V.J. 1999 ISEM-6: Infrared Surface Emissivity Model for RTTOV-6. *NWP Tech. Rep. 287 (available from* *http://www.metoffice.com/research/interproj/nwpsaf/rtm/rtm_reports.html* *).*

Strow, L.L., H.E. Motteler, R.G. Benson, S.E. Hannon, and S. De Souza-Machado. 1998 Fast computation of monochromatic infrared atmospheric transmittances using compressed look-up tables. *J. Quant. Spectrosc. Rad. Trans.*, **59**, *481-493*.

Wyser, K., 1998: The effective radius in cirrus clouds. *J. Clim.*, **11,** *1793-1802*.

Predictor	Fixed gases	Water vapour (line+continuum)	Ozone
$X_{j,1}$	$sec(\theta)$	$sec^2(\theta)W_r^2(j)$	$sec(\theta)O_r(j)$
$X_{j,2}$	$sec^2(\theta)$	$(sec(\theta)W_w(j))^2$	$\sqrt{sec(\theta)O_r(j)}$
$X_{j,3}$	$sec(\theta)T_r(j)$	$(sec(\theta)W_w(j))^4$	$sec(\theta)O_r(j)\delta T(j)$
$X_{j,4}$	$sec(\theta)T_r^2(j)$	$sec(\theta)W_r(j)\delta T(j)$	$(sec(\theta)O_r(j))^2$
$X_{j,5}$	$T_r(j)$	$\sqrt{sec(\theta)W_r(j)}$	$\sqrt{sec(\theta)O_r(j)}\ \delta T(j)$
$X_{j,6}$	$T_r^2(j)$	$\sqrt[4]{sec(\theta)W_r(j)}$	$sec(\theta)O_r(j)^2O_w(j)$
$X_{j,7}$	$sec(\theta)T_w(j)$	$sec(\theta)W_r(j)$	$\frac{O_r(j)}{O_w(j)}\sqrt{sec(\theta)O_r(j)}$
$X_{j,8}$	$sec(\theta)\frac{T_w(j)}{T_r(j)}$	$(sec(\theta)W_r(j))^3$	$sec(\theta)O_r(j)O_w(j)$
$X_{j,9}$	$\sqrt{sec(\theta)}$	$(sec(\theta)W_r(j))^4$	$O_r(j)sec(\theta)\sqrt{(O_w(j)sec(\theta)}$
$X_{j,10}$	$\sqrt{sec(\theta)}\ \sqrt[4]{T_w(j)}$	$sec(\theta)W_r(j)\delta T(j)\lvert\delta T(j)\rvert$	$sec(\theta)O_w(j)$
$X_{j,11}$	0	$(\sqrt{sec(\theta)W_r(j)}\ )\delta T(j)$	$(sec(\theta)O_w(j))^2$
$X_{j,12}$	0	$\frac{sec(\theta)(W_r(j))^2}{W_w}$	0
$X_{j,13}$	0	$\frac{\sqrt{(sec(\theta)W_r(j)}W_r(j)}{W_w(j)}$	0
$X_{j,14}$	0	$sec(\theta)\frac{W_r^2(j)}{T_r(j)}$	0
$X_{j,15}$	0	$sec(\theta)\frac{W_r^2(j)}{T_r^4(j)}$	0

Table 1. Predictors used by RTTOV-7 for Fixed Gases, Water Vapour and Ozone

Predictor	Fixed gases	Water vapour (line)	Ozone (optional)
$X_{j,1}$	$sec(\theta)$	$sec^2(\theta)W_r^2(j)$	$sec(\theta)O_r(j)$
$X_{j,2}$	$sec^2(\theta)$	$(\sec(\theta)W_w(j))$	$\sqrt{sec(\theta)O_r(j)}$
$X_{j,3}$	$sec(\theta)T_r(j)$	$(\sec(\theta)W_w(j))^2$	$sec(\theta)O_r(j)\delta T(j)$
$X_{j,4}$	$sec(\theta)T_r^2(j)$	$sec(\theta)W_r(j)\delta T(j)$	$(sec(\theta)O_r(j))^2$
$X_{j,5}$	$T_r(j)$	$\sqrt{sec(\theta)W_r(j)}$	$\sqrt{sec(\theta)O_r(j)}\ \delta T(j)$
$X_{j,6}$	$T_r^2(j)$	$\sqrt[4]{sec(\theta)W_r(j)}$	$sec(\theta)O_r(j)^2O_w(j)$
$X_{j,7}$	$sec(\theta)T_w(j)$	$sec(\theta)W_r(j)$	$\frac{O_r(j)}{O_w(j)}\sqrt{sec(\theta)O_r(j)}$
$X_{j,8}$	$sec(\theta)\frac{T_w(j)}{T_r(j)}$	$(sec(\theta)W_r(j))^3$	$sec(\theta)O_r(j)O_w(j)$
$X_{j,9}$	$\sqrt{sec(\theta)}$	$sec(\theta)W_r(j)\delta T(j)\lvert\delta T(j)\rvert$	$O_r(j)sec(\theta)\sqrt{(O_w(j)sec(\theta)}$
$X_{j,10}$	$\sqrt{sec(\theta)}\ \sqrt[4]{T_w(j)}$	$(\sqrt{sec(\theta)W_r(j)})\delta T(j)$	$sec(\theta)O_w(j)$
$X_{j,11}$	0	$\sec(\theta)\frac{W_r^2(j)}{W_{tw}(j)}$	$(sec(\theta)O_w(j))^2$
$X_{j,12}$	0	$\frac{\sqrt{(\sec(\theta)W_r(j)}W_r(j)}{W_{tw}(j)}$	0

Table 2. Predictors used by RTTOV-8 for Fixed Gases, Water Vapour (line) and Ozone

Predictor	Water vapour (continuum)	Carbon dioxide (optional)
$X_{j,1}$	$\sec(\theta)\frac{W_r^2(j)}{T_r(j)}$	$\sec(\theta)CO2_r(j)$
$X_{j,2}$	$\sec(\theta)\frac{W_r^2(j)}{T_r^4(j)}$	$T_r^2(j)$
$X_{j,3}$	$\sec(\theta)\frac{W_r(j)}{T_r(j)}$	$\sec(\theta)T_r(j)$
$X_{j,4}$	$\sec(\theta)\frac{W_r(j)}{T_r^2(j)}$	$\sec(\theta)T_r^2(j)$
$X_{j,5}$		$T_r(j)$
$X_{j,6}$		$\sec(\theta)$
$X_{j,7}$		$\sec(\theta)T_{wr}(j)$
$X_{j,8}$		$(\sec(\theta)CO2_w(j))^2$
$X_{j,9}$		$T_{wr}^3(j)$
$X_{j,10}$		$\sec(\theta)T_{wr}(j)\sqrt{T_r}$

Table 3. Predictors used by RTTOV-8 for Water Vapour (continuum) and Carbon Dioxide

$$T(l) = [T^{profile}(l) + T^{profile}(l-1)] / 2 \qquad T^{*}(l) = [T^{reference}(l) + T^{reference}(l-1)] / 2$$
$$W(l) = [W^{profile}(l) + W^{profile}(l-1)] / 2 \qquad W^{*}(l) = [W^{reference}(l) + W^{reference}(l-1)] / 2$$
$$O(l) = [O^{profile}(l) + O^{profile}(l-1)] / 2 \qquad O^{*}(l) = [O^{reference}(l) + O^{reference}(l-1)] / 2$$
$$CO_2(l) = [CO_2{}^{profile}(l) + CO_2{}^{profile}(l-1)] / 2 \qquad CO_2{}^{*}(l) = [CO_2{}^{reference}(l) + CO_2{}^{reference}(l-1)] / 2$$
$$T(1) = T^{profile}(1) \qquad W(1) = W^{profile}(1) \qquad O(1) = O^{profile}(1) \qquad CO_2(1) = CO_2{}^{profile}(1)$$
$$P(l) = Pres(l)$$

$$T_r(l) = T(l) / T^{*}(l) \qquad \delta T(l) = T(l) - T^{*}(l) \qquad W_r(l) = W(l) / W^{*}(l)$$
$$O_r(l) = O(l) / O^{*}(l) \qquad CO_{2r}(l) = CO_2(l) / CO_2{}^{*}(l)$$

$$T_w(l) = \sum_{i=2}^{l} P(i)\,[P(i) - P(i-1)]\,T_r(i-1)$$
$$T_{wr}(l) = \left\{\sum_{i=1}^{l} P(i)\,[P(i) - P(i-1)]\,T(i-1)\right\} \Big/ \left\{\sum_{i=1}^{l} P(i)\,[P(i) - P(i-1)]\,T^{*}(i-1)\right\}$$
$$W_w(l) = \{\sum_{i=1}^{l} P(i)\,[P(i) - P(i-1)]\,W(i)\} / \{\sum_{i=1}^{l} P(i)\,[P(i) - P(i-1)]\,W^{*}(i)\}$$
$$W_{tw}(l) = \{\sum_{i=1}^{l} P(i)\,[P(i) - P(i-1)]\,W(i).T(i)\} / \{\sum_{i=1}^{l} P(i)\,[P(i) - P(i-1)]\,W^{*}(i).T^{*}(i)\}$$
$$O_w(l) = \{\sum_{i=1}^{l} P(i)\,[P(i) - P(i-1)]\,O(i)\} / \{\sum_{i=1}^{l} P(i)\,[P(i) - P(i-1)]\,O^{*}(j)\}$$
$$CO_{2w}(l) = \{\sum_{i=1}^{l} P(i)\,[P(i) - P(i-1)]\,CO_2(i)\} / \{\sum_{i=1}^{l} P(i)\,[P(i) - P(i-1)]\,CO_2{}^{*}(j)\}$$

The $Pres(l)$'s are the values of the pressure at each level.
$T^{profile}(l), W^{profile}(l)$ and $O^{profile}(l)$ are the temperature, water vapour mixing ratio and ozone mixing ratio profiles at each level. $T^{reference}(l), W^{reference}(l)$ and $O^{reference}(l)$ are corresponding reference profiles. For these variables l refers to the lth level. In all other cases l is the lth layer (which is above the lth level). For the 43 level profiles $Pres(1) =$ 0.1hPa that coincides with the lower boundary of layer 1 (bounded by 0.005 and 0.1 hPa).

Table 4. Definition of profile variables used in predictors defined in Tables 1, 2, 3.

HIRS		RTTOV-8 117 independent set		
Channel #	NeDT degK	Mean bias degK	St. dev. degK	Max diff degK
1	2.77	0.00	0.03	0.12
2	0.74	-0.01	0.01	0.06
3	0.55	0.00	0.01	0.06
4	0.31	0.01	0.02	0.13
5	0.18	0.03	0.03	0.21
6	0.18	0.01	0.03	0.11
7	0.14	0.01	0.05	0.20
8	0.06	0.00	0.01	0.09
9	0.13	0.08	0.09	0.25
10	0.17	-0.03	0.06	0.30
11	0.44	-0.04	0.09	0.35
12	0.96	-0.06	0.14	1.00
13	0.10	0.01	0.02	0.11
14	0.10	0.01	0.02	0.06
15	0.24	0.01	0.02	0.09
16	0.31	0.02	0.02	0.10
17	0.15	0.01	0.01	0.04
18	0.04	0.00	0.01	0.02
19	0.02	0.00	0.02	0.10

Table 5. NOAA-15 HIRS brightness temperature statistics for RTTOV-8 minus LbL values for ECMWF 117 independent profile sets for 5 angles out to 60 deg.

AMSU-A		RTTOV-8 117 independent set		
Channel #	NeDT degK	Mean bias degK	St. dev. degK	Max diff degK
1	0.20	0.00	0.01	0.04
2	0.24	-0.01	0.02	0.12
3	0.19	-0.02	0.03	0.18
4	0.13	0.01	0.01	0.07
5	0.13	0.02	0.01	0.08
6	0.11	0.01	0.01	0.06
7	0.12	0.00	0.01	0.03
8	0.13	0.00	0.00	0.01
9	0.15	-0.01	0.01	0.07
10	0.19	0.19	0.16	0.39
11	0.20	0.00	0.04	0.27
12	0.31	-0.02	0.07	0.44
13	0.42	-0.05	0.09	0.58
14	0.70	-0.04	0.06	0.41
15	0.10	0.07	0.10	0.34

Table 6. NOAA-15 AMSU-A brightness temperature statistics for RTTOV-8 minus LbL values for ECMWF 117 independent profile sets for 5 angles out to 60 deg.

AMSU-B		RTTOV-8 117 independent set		
Channel #	NeDT degK	Mean bias degK	St. dev. degK	Max diff degK
1	0.32	0.07	0.10	0.33
2	0.71	-0.02	0.08	0.73
3	1.05	-0.01	0.07	0.74
4	0.69	-0.01	0.04	0.44
5	0.57	0.00	0.05	0.40

Table 7. NOAA-15 AMSU-B brightness temperature statistics for RTTOV-8 minus LbL values for ECMWF 117 independent profile sets for 5 angles out to 60 deg.

SEVIRI	RTTOV-8 117 independent set		
Channel # (wavelength)	Mean bias degK	St. dev. degK	Max diff degK
4 3.9μm	0.00	0 .01	0.08
5 6.2μm	-0.07	0.18	1.07
6 7.3μm	-0.03	0.11	0.37
7 8.7μm	-0.01	0.04	0.28
8 9.7μm	0.06	0.09	0.26
9 10.8μm	0.00	0.01	0.08
10 12.0μm	-0.01	0.03	0.20
11 13.4μm	-0.12	0.08	0.34

Table 8 Meteosat-8 SEVIRI brightness temperature difference statistics for RTTOV-8 minus LbL values for ECMWF 117 independent profile set. The surface emissivity was set to unity and the values include 6 zenith angles from zero to 63.6 deg.

Model	RTTOV-7	RTTOV-7 PW	MODTRAN-4	RAD7.4.3
SEVIRI Channel #	Nadir (Model-RFM)			
4 (3.9μm)	1.76(0.13)	-0.09(0.05)	0.14(0.04)	0.02(0.04)
7 (8.7μm)	-0.11(0.09)	-0.08(0.08)	-0.22(0.12)	-0.36(0.11)
9 (10.8μm)	-0.04(0.02)	-0.05(0.03)	-0.03(0.10)	0.00(0.10)
10 (12.0μm)	0.00(0.04)	-0.02(0.04)	-0.06(0.15)	0.07(0.14)
	60 deg (Model-RFM)			
4 (3.9μm)	2.15(0.20)	-0.07(0.07)	-0.03(0.07)	0.10(0.08)
7 (8.7μm)	0.03(0.17)	0.02(0.17)	-0.57(0.24)	-0.60(0.20)
9 (10.8μm)	0.05(0.09)	0.04(0.10)	-0.14(0.16)	0.00(0.12)
10 (12.0μm)	0.09(0.10)	0.07(0.10)	-0.20(0.21)	0.04(0.15)

Table 9. Brightness temperature differences in deg K between RT model and RFM for 58 ECMWF diverse profiles over the sea. The mean bias and standard deviation in brackets are listed.

Model	AMSU-06		AMSU-10		AMSU-14		AMSU-18	
	std	bias	std	bias	std	bias	std	bias
RTTOV-7/8	0.04	-0.06	0.15	0.25	**1.36**	0.90	**0.35**	-0.39
OPTRAN	0.09	0.00	0.05	-0.04	**0.73**	-1.97	0.10	0.00
AER_OSS	0.06	0.13	0.04	0.03	0.09	0.14	0.14	-0.16
MIT	0.01	0.00	0.04	-0.04	0.08	-0.09	0.19	-0.40
RAYTHEON	**0.42**	-0.57	0.17	0.24	0.20	0.60	**0.50**	-0.07
AER_LBL	0.06	0.13	0.05	0.03	0.09	0.16	0.14	-0.15
MSCMWLBL	0.03	0.05	0.03	0.04	0.20	0.51	**0.32**	-0.36
ATM	0.19	0.46	0.07	0.08	0.11	0.23	0.24	-0.28

Table 10. Brightness temperature standard deviation and bias of various models against the CIMSS MWLBL model for the 4 AMSU channels standard deviations above 0.25K are in bold (adapted from Garand et. al. 2001).

Channel Number	AIRS channel	Frequency cm^{-1}	Jacobian computed
1	71	666.7	T
2	77	668.2	T
3	305	737.1	T
4	453	793.1	T, Q
5	672	871.2	T, Q
6	787	917.2	T
7	1021	1009.2	T, O_3
8	1090	1040.1	O_3
9	1142	1074.3	Q
10	1437	1323.8	Q
11	1449	1330.8	Q
12	1627	1427.1	Q
13	1766	1544.3	Q
14	1794	1563.5	Q
15	1812	1576.1	Q
16	1917	2229.3	T
17	1958	2268.7	T
18	1995	2305.5	T
19	2107	2385.9	T
20	2197	2500.3	T

Table 11. AIRS channels used for jacobian validations

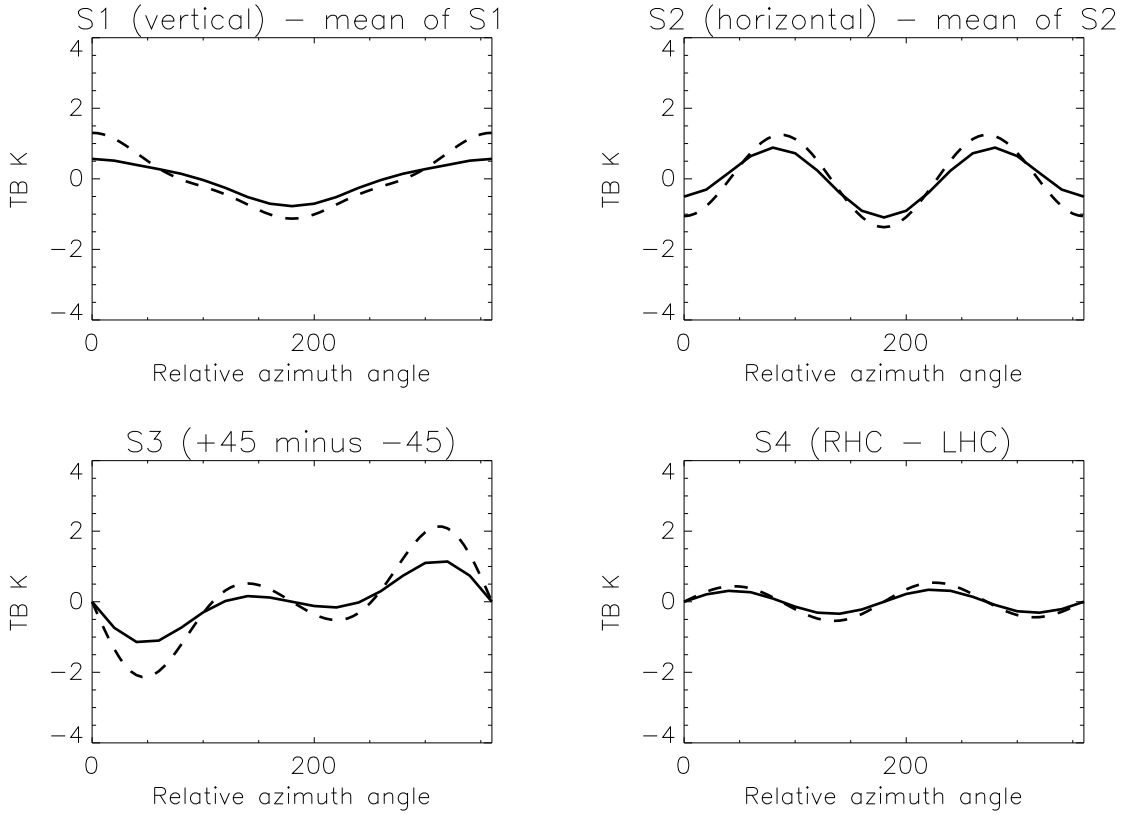

Figure 1: Comparison of azimuthal brightness temperature dependence from the fast model of Liu (dashed) and the model of Coppo et al. 1996 (continuous). Frequency = 37 GHz, windspeed = 8.7 ms^{-1}, sea surface temperature = 293 K, view angle = 55^o.

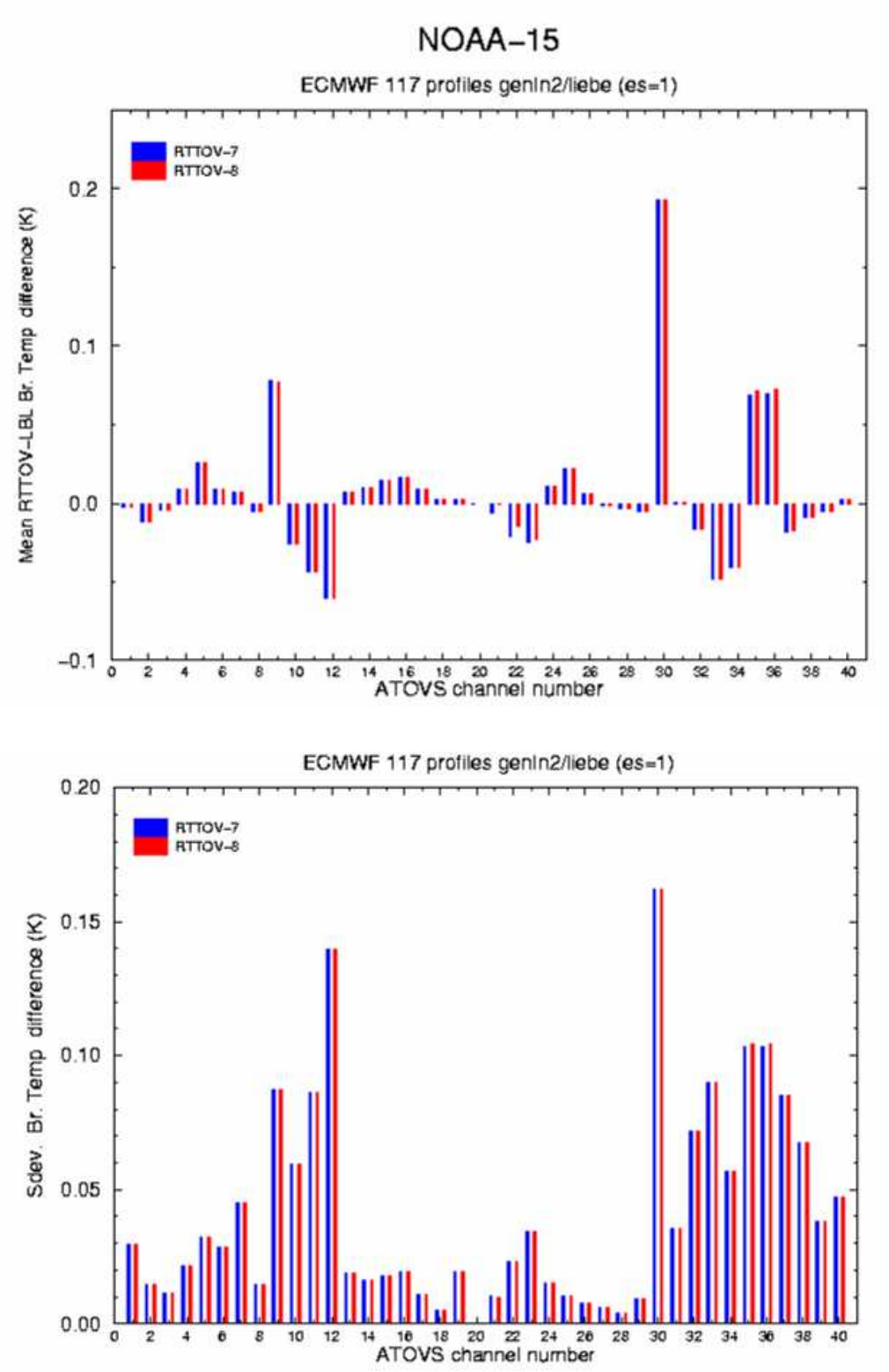

Figure 2. Comparison of mean bias (upper panel) and standard deviation (lower panel) of RTTOV-7 and 8 brightness temperature differences from Line by Line calculations for 5 viewing angles for 117 independent profile sets for NOAA-15 ATOVS. Channels 1-19 = HIRS; 21-35=AMSU-A; 36-40=AMSU-B. The RT integration over layers is identical for both LbL and RTTOV models. The surface emissivity was specified for these comparisons.

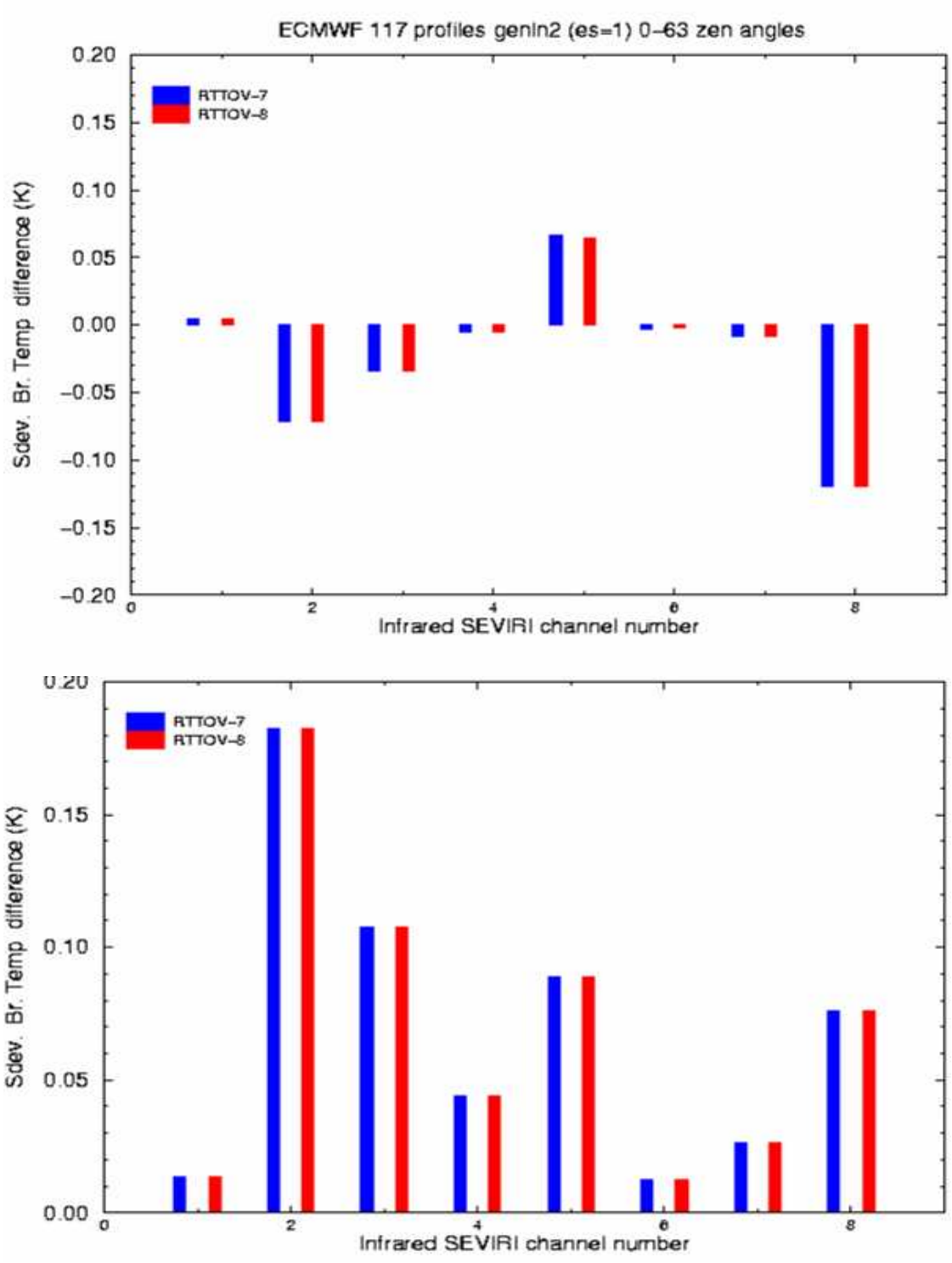

Figure 3. Comparison of mean bias (upper panel) and standard deviation (lower panel) of RTTOV-7 and 8 brightness temperature differences from Line by Line calculations for 6 viewing angles for 117 independent profile sets forMeteosat-8 SEVIRI. The RT integration over layers is identical for both LbL and RTTOV models. The surface emissivity was specified for these comparisons.

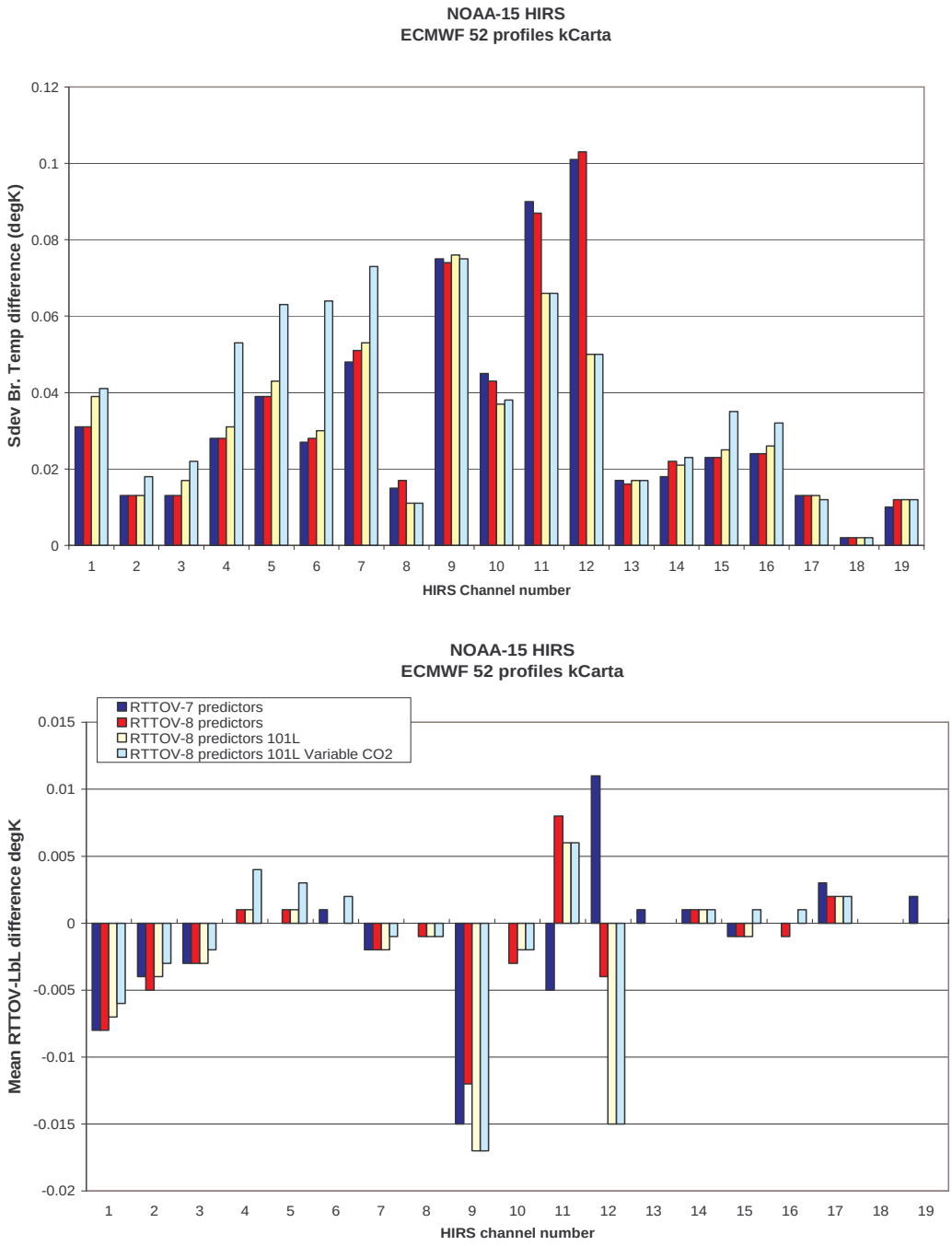

Figure 4. Comparison of RTTOV-7 on 43 levels and RTTOV-8 optical depth predictors as defined in Tables 2 & 3 on 43 levels and 101 levels with and without variable CO_2. The differences are computed for 52 diverse profiles, 6 viewing angles with kCarta as the LbL model for all coefficients. Dark blue are RTTOV-7 predictors, red are RTTOV-8 predictors yellow are RTTOV-8 predictors on 101 levels and light blue are with variable CO_2.

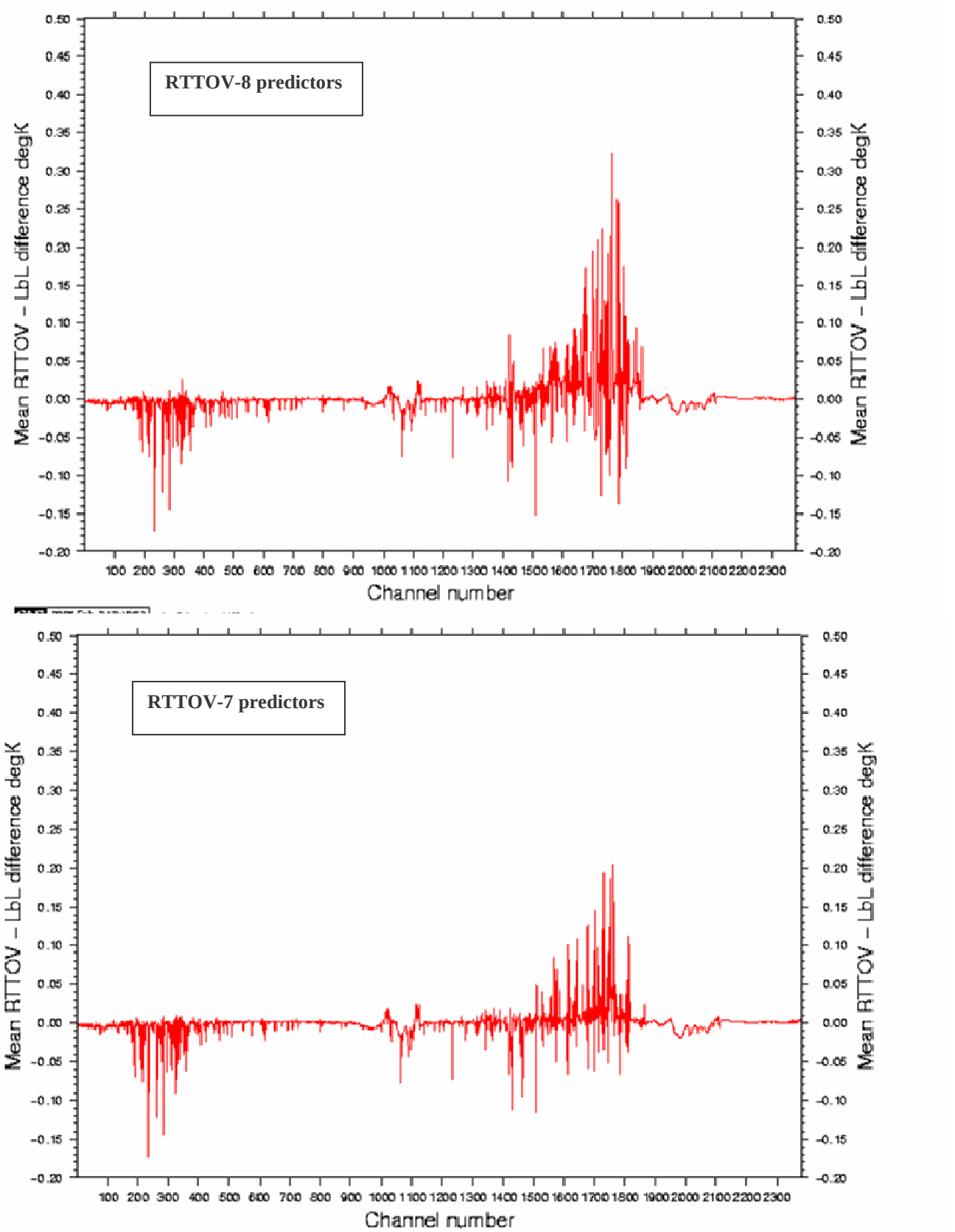

Figure 5. Mean bias for AIRS channels with RTTOV-8 optical depth predictors (top panel) and RTTOV-7 predictors (bottom panel). The RT integration is the same for LbL and RTTOV simulations.

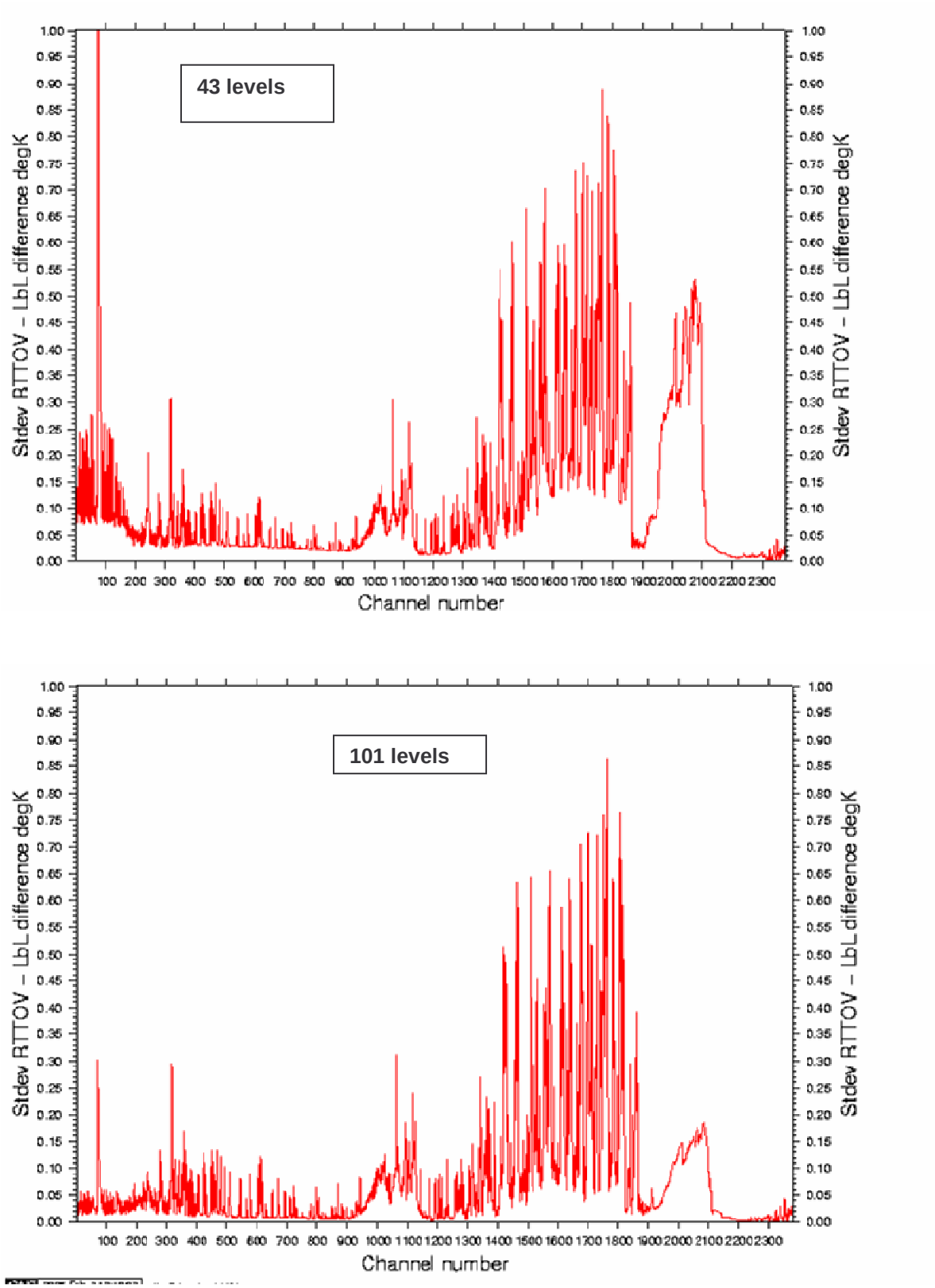

Figure 6. Effect of number of levels on the standard deviation of the difference between the LbL model and RTTOV-8 for AIRS. The top panel shows the standard deviation of the differences for 43 levels and the bottom panel shows the same for 101 levels.

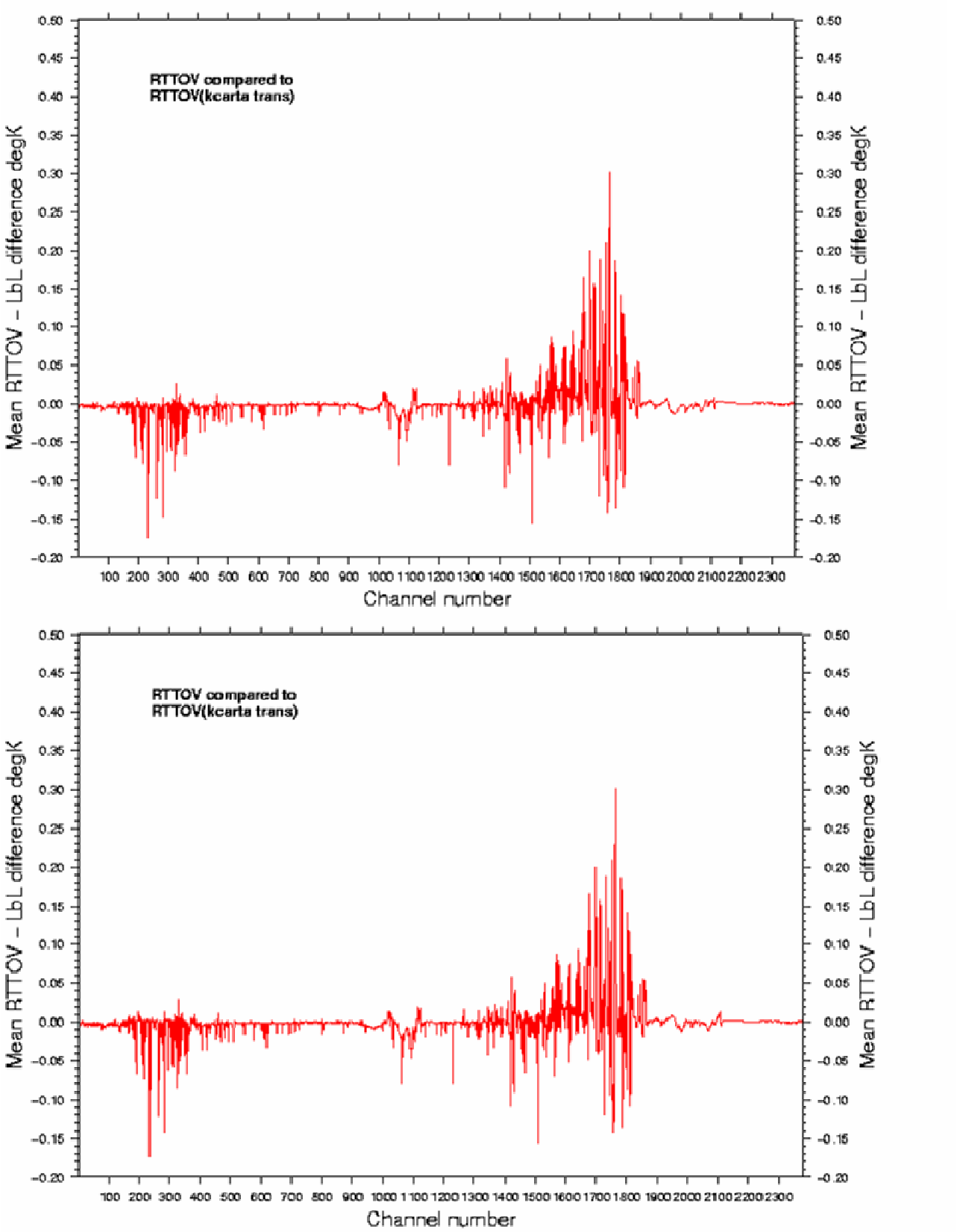

Figure 7. Comparison of the difference between the LbL model and RTTOV-8 for AIRS for fixed CO_2 and variable CO_2. The top panel shows the differences for fixed CO_2 and the bottom panel shows the same for variable CO_2 on 101 levels.

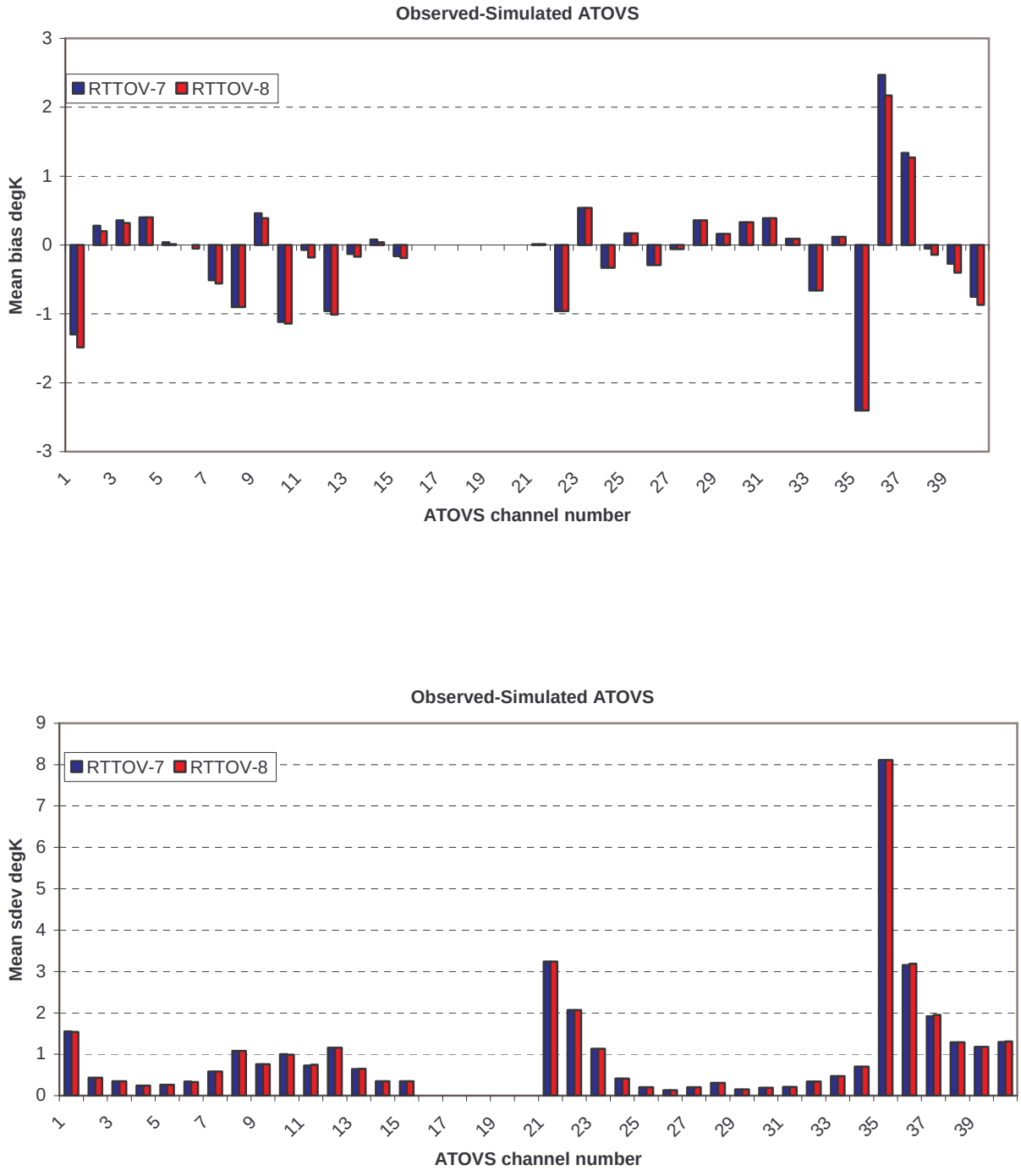

Figure 8. Comparison between observed minus simulated ATOVS radiances using the ECMWF model and RTTOV-7 and 8. The period of the comparison was for 21 days in March 2004.

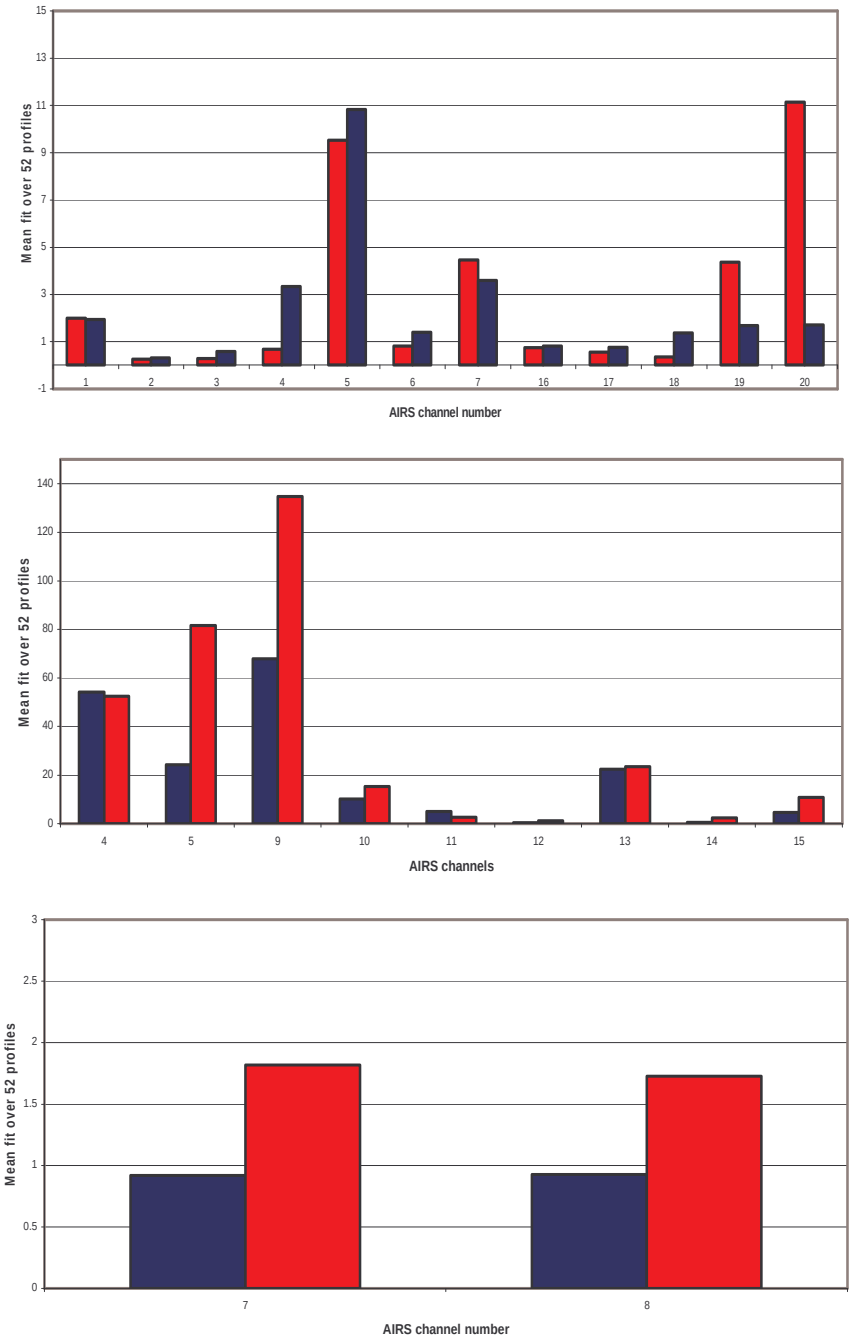

Figure 9. A summary of the mean fit of the RTTOV temperature (top panel), water vapour jacobians (middle panel)and ozone (lower panel) to RFM for the AIRS channel numbers defined in Table 11. Blue is RTTOV-8 and red is RTTOV-7.

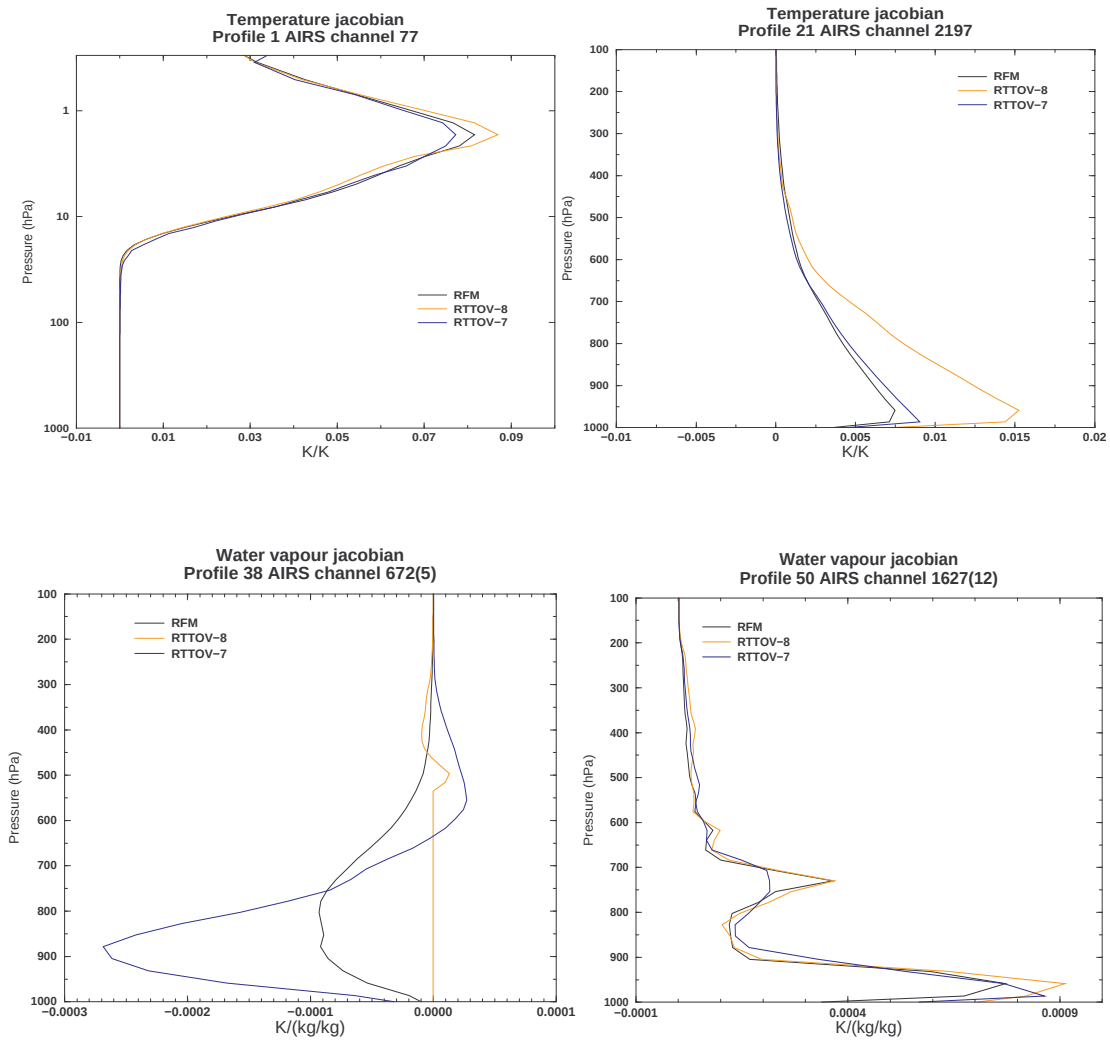

Figure 10. Some examples of temperature jacobians (top panels) and water vapour jacobians (lower panels) for RTTOV-7 and 8 compared with RFM.

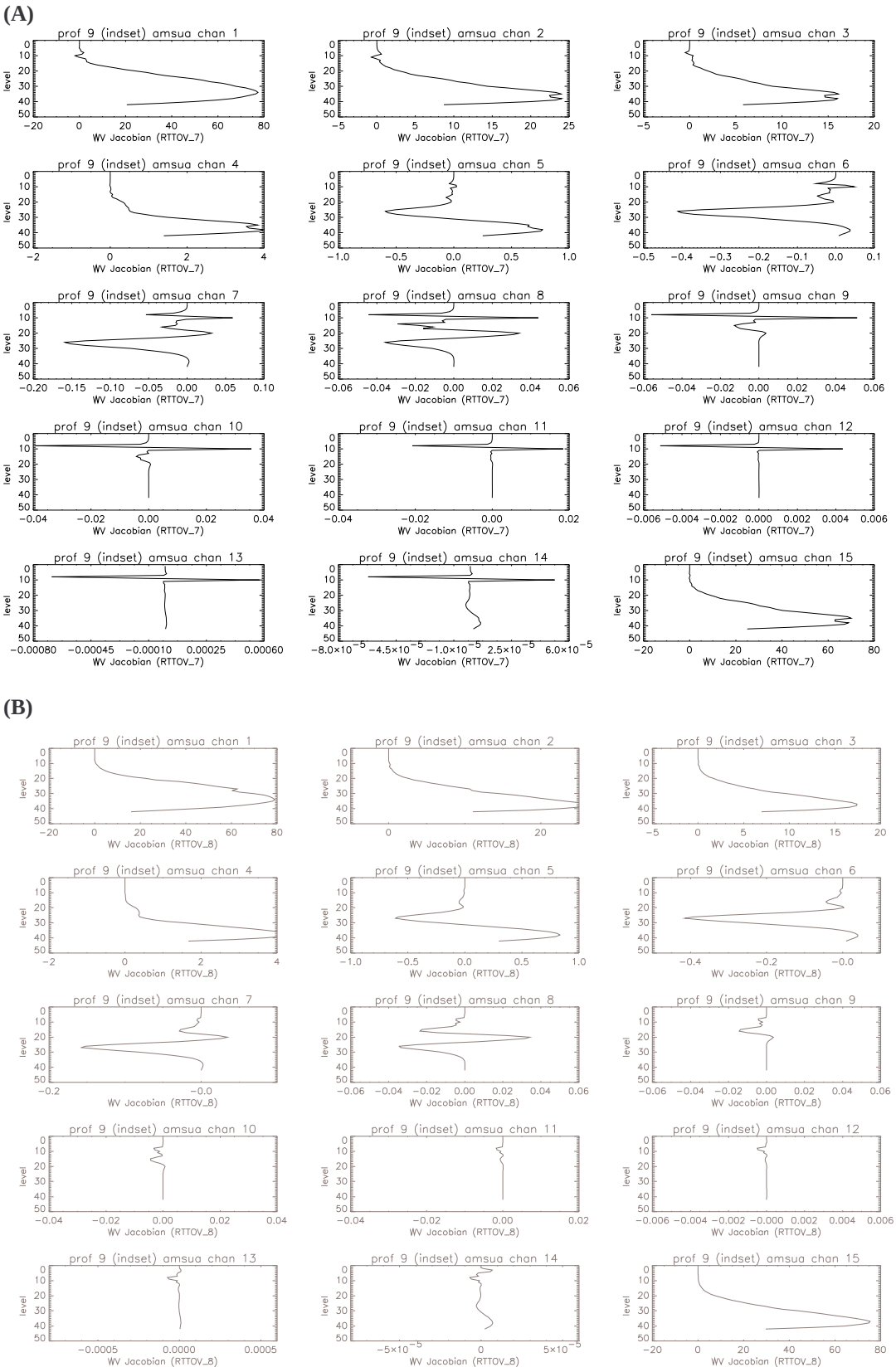

Figure 11. AMSU-A water vapour jacobians computed from profile 9 of the 117 independent profile set for RTTOV-7 predictors (A) and RTTOV-8 predictors (B).

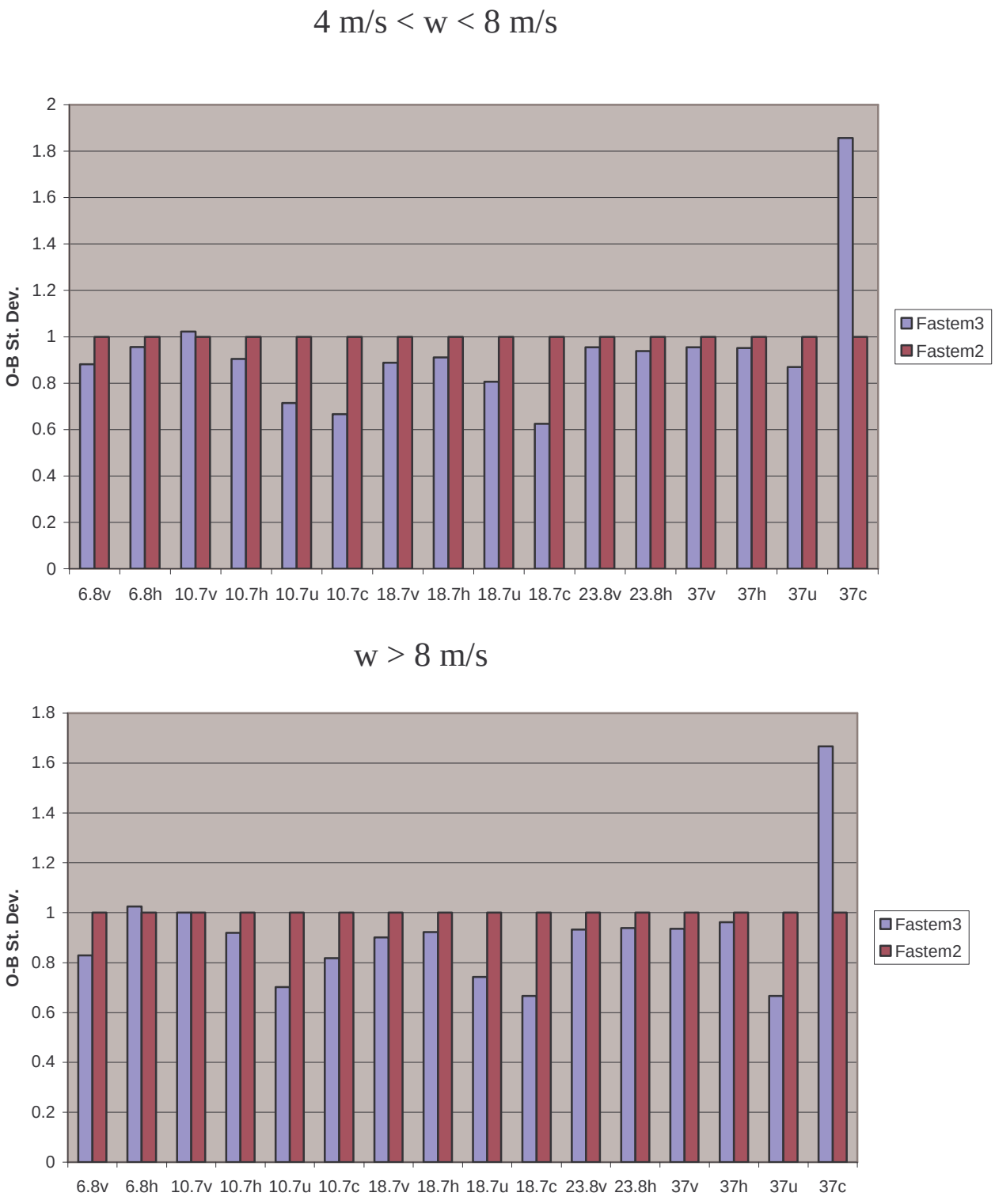

Figure 12. Improved fit of RTTOV-8 radiances to Coriolis Windsat channels in terms of percentage for FASTEM-3 relative to FASTEM-2. The upper panel is for wind speeds between 4 to 8 m.s^{-1} and the lower panel is for wind speeds greater than 8 m.s^{-1}. Note the 37 GHz circular polarised channel is broken.

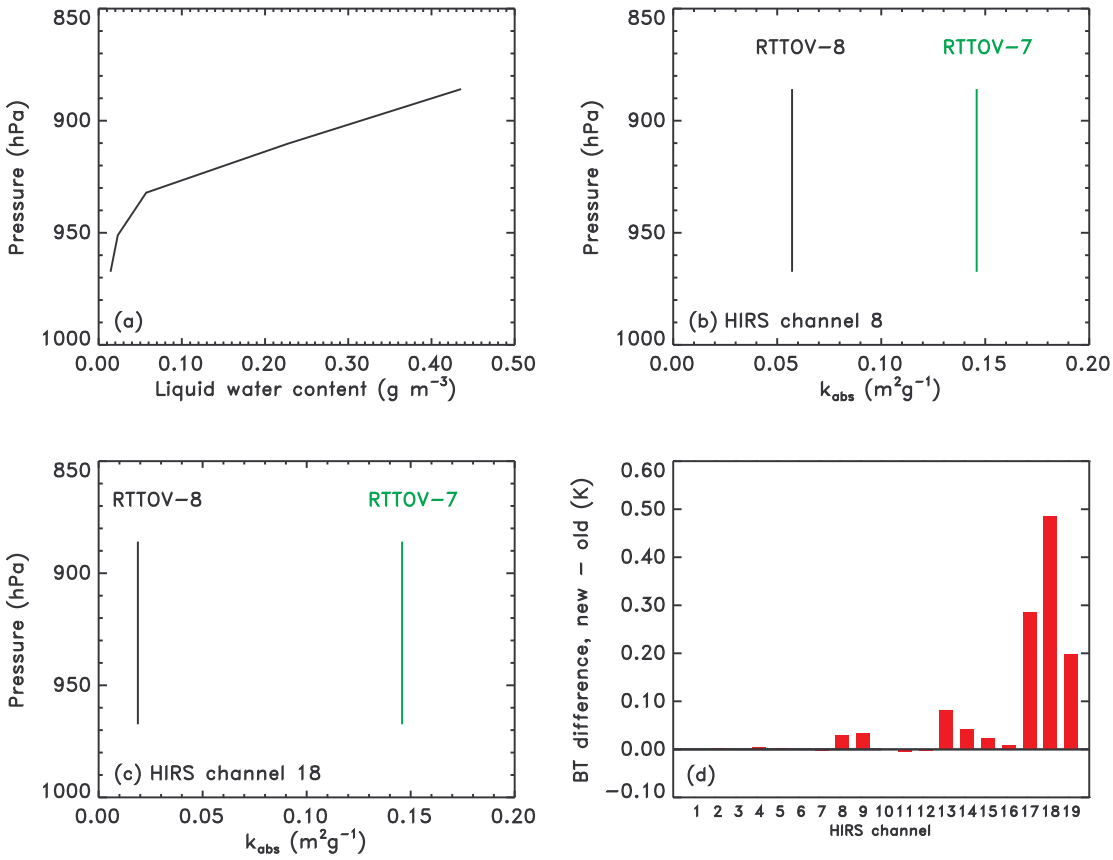

Figure 13. A comparison of the HIRS channels for water cloud radiance simulations for RTTOV-7 and 8. The top LH panel shows the water content profile, the top RH panel the absorption coefficients assigned for the 2 models for HIRS channel 8 and for HIRS channel 18 (lower LH panel) and the lower RH panel shows the brightness temperature differences for all the HIRS channels between RTTOV-7 and RTTOV-8.

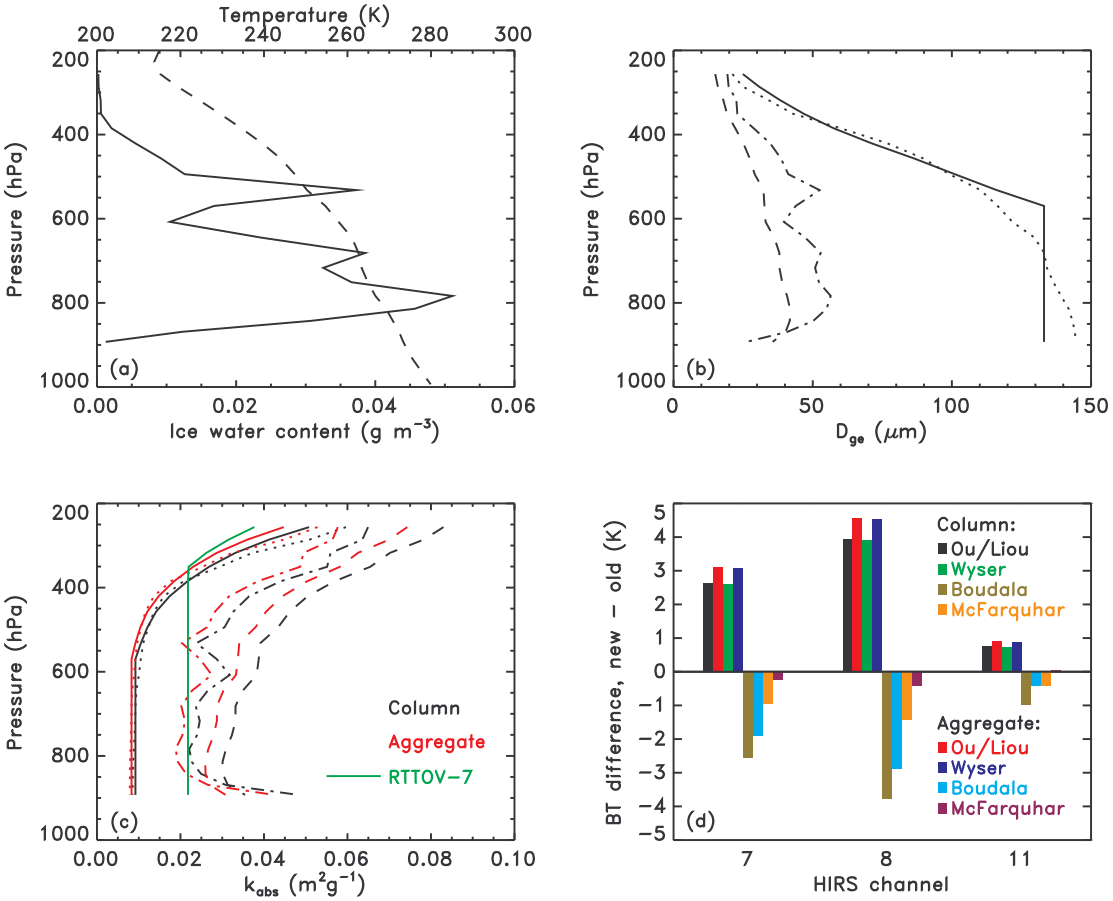

Figure 14. A comparison of the HIRS channels for ice cloud radiance simulations for RTTOV-7 and 8. The top LH panel shows the temperature and ice water content profile, the top RH panel the diagnosed ice crystal effective radius for the various parametrisations available in RTTOV-8. The lower LH panel shows the absorption coefficients for column and aggregates and the lower RH panel the HIRS channel brightness temperature differences for each of the paremetrisations. The dotted line is Wyser (1998), the solid line Ou and Liou (1995), the dashed line Boudala et. al. (2002) and the dot-dashed line McFarquar (2003).

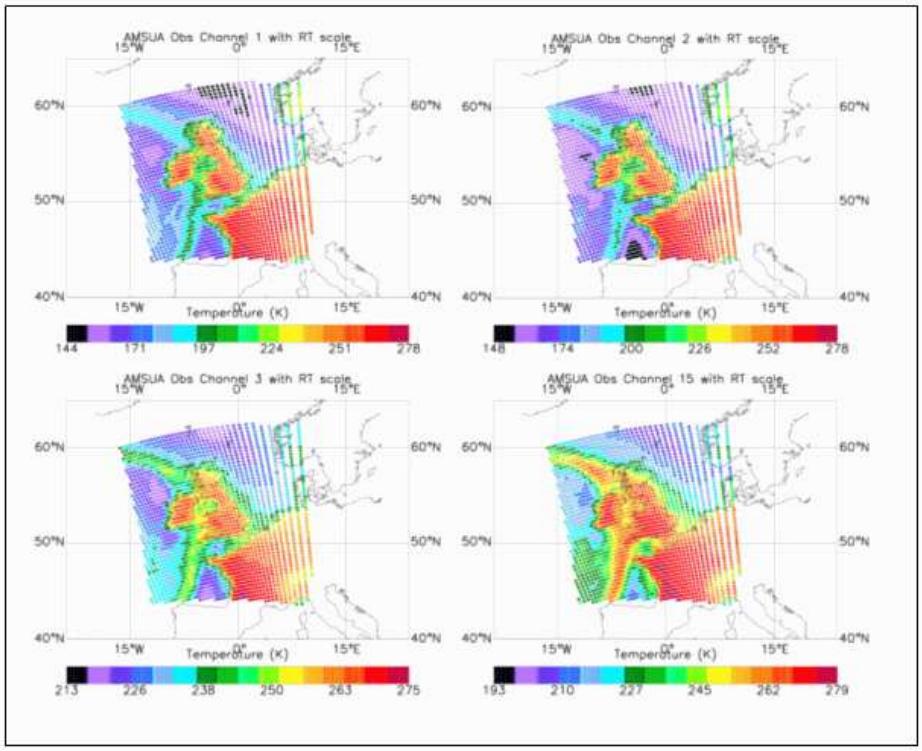

Fig 15a: NOAA-16 observed brightness temperatures at 13Z at 25/01/02 at (clockwise from top left) 21.8GHz, 31.4GHz, 50.3GHz and 89.0GHz

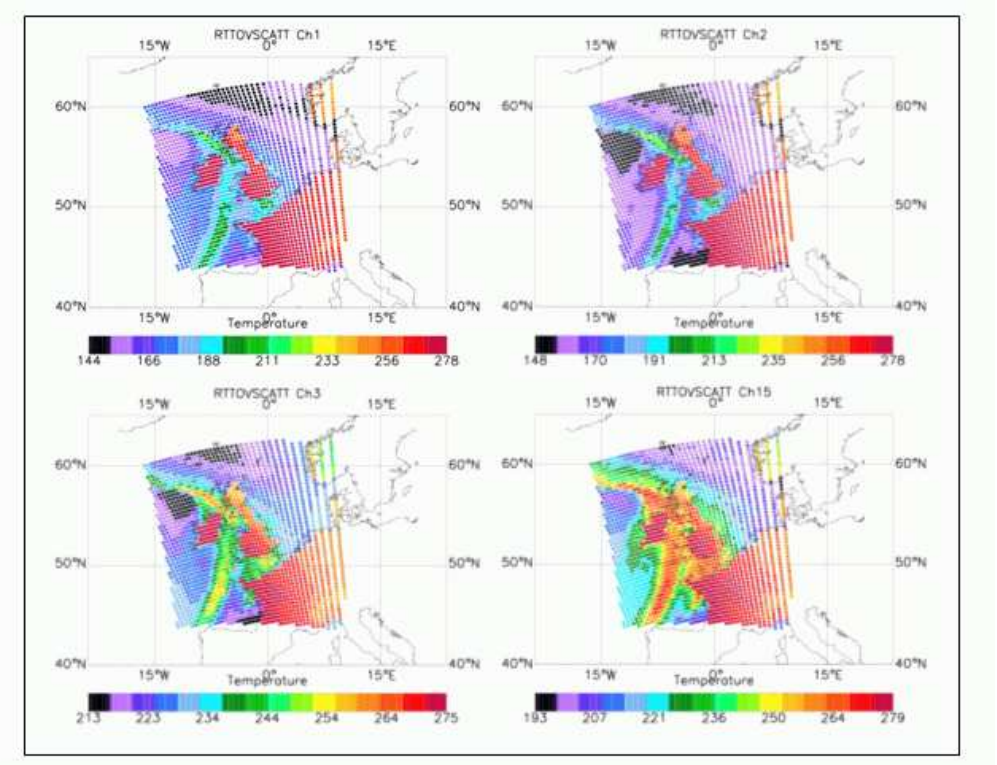

Fig 15b: RTTOVSCATT simulated brightness temperatures using Met Office Mesoscale Model input profiles at (clockwise from top left) 21.8GHz, 31.4GHz, 50.3GHz and 89.0GHz

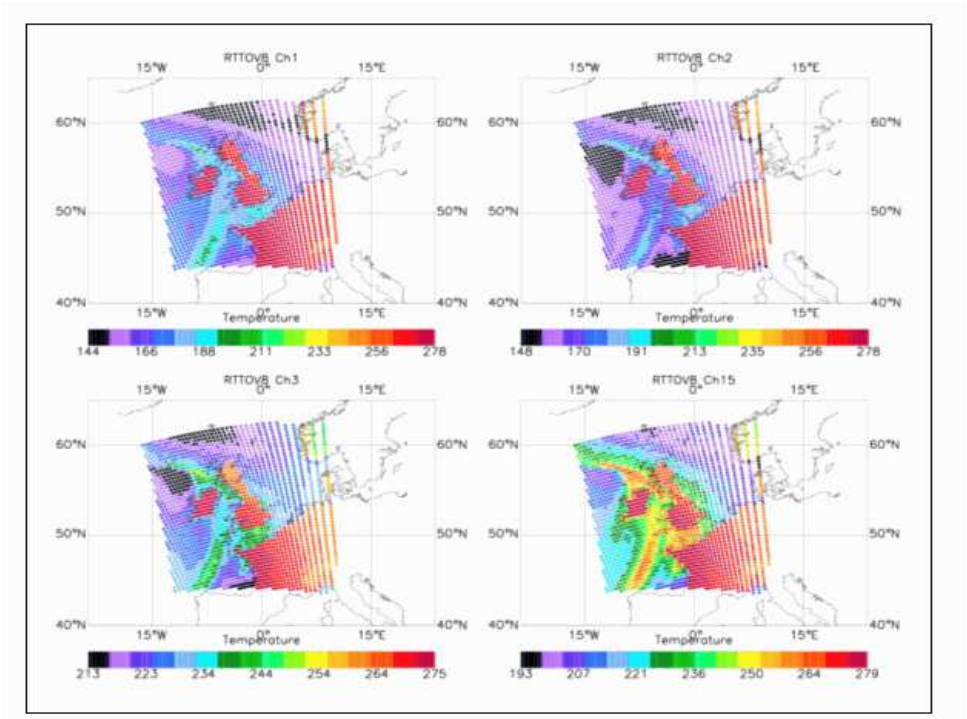

Fig 15c: RTTOV-8 simulated brightness temperatures using Met Office Mesoscale Model input profiles at (clockwise from top left) 21.8GHz, 31.4GHz, 50.3GHz and 89.0GHz including LWP path in the profile.

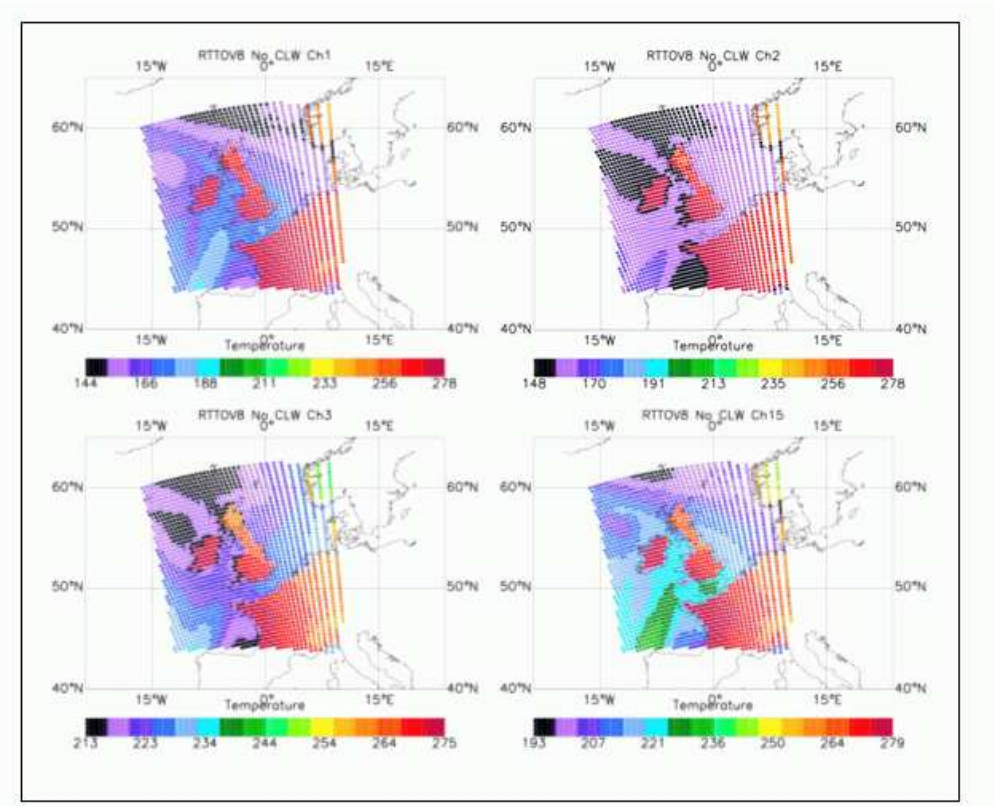

Fig 15d: RTTOV-8 simulated brightness temperatures (ignoring liquid water emission effects) using Met Office Mesoscale Model input profiles at (clockwise from top left) 21.8GHz, 31.4GHz, 50.3GHz and 89.0GHz

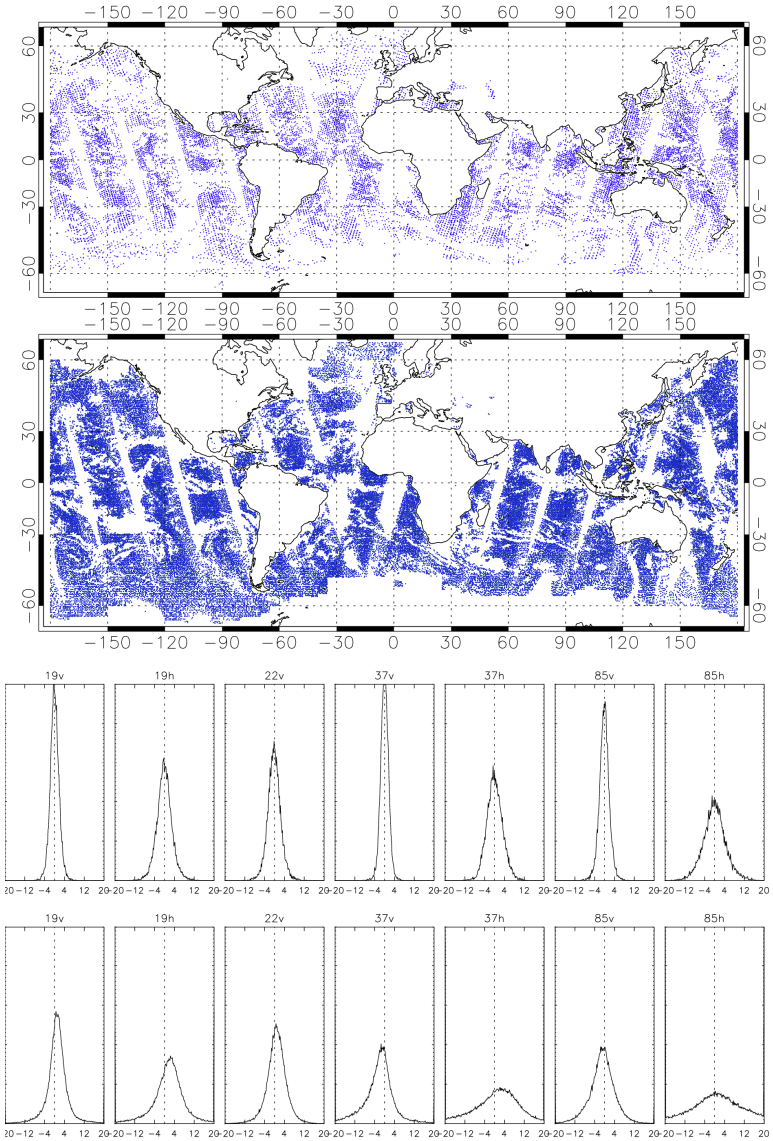

Figure 16. Coverage for a 12 hour observation window on August 3, 2004 (00 UTC analysis) of DMSP F-13/14/15 SSM/I clear-sky observations (a; pre-thinned, screened for clouds and precip), cloud/precip observations (b; no pre-thinning), first-guess departures of clear-sky (c) and precipitation observations (d) for 7 SSM/I channels.

End of Report